A NOVEL METHOD FOR THERMAL CONDUCTIVITY MEASUREMENT OF TWO DIMENSIONAL MATERIALS

A THESIS SUBMITTED TO
THE GRADUATE SCHOOL OF ENGINEERING AND SCIENCE
OF BILKENT UNIVERSITY
IN PARTIAL FULFILLMENT OF THE REQUIREMENTS FOR
THE DEGREE OF
MASTER OF SCIENCE
IN
DEPARTMENT OF PHYSICS

By
Onur Çakıroğlu
September 2019

A Novel Method for Thermal Conductivity Measurement of Two Dimensional Materials
By Onur Çakıroğlu
September 2019

We certify that we have read this thesis and that in our opinion it is fully adequate, in scope and in quality, as a thesis for the degree of Master of Science.

Talip Serkan Kasırga(Advisor)

Mehmet Özgür Oktel

Evren Mutlugün

Approved for the Graduate School of Engineering and Science:

Ezhan Karaşan
Director of the Graduate School

ABSTRACT

A NOVEL METHOD FOR THERMAL CONDUCTIVITY MEASUREMENT OF TWO DIMENSIONAL MATERIALS

Onur Çakıroğlu
M.S. in Department of Physics
Advisor: Talip Serkan Kasırga
September 2019

Thermal conductivity is a quantity which governs the heat transfer in a material. After increasing importance of efficiency in power generation systems and cooling mechanisms in micro-structures, many measurement methods have been developed to explore the thermal conductivity in micro and nano-sized materials. However, complexity in experimental setups, difficulties in the fabrication of devices required for measurements, and lacking exact solutions to thermal equations limit the usability of the methods to a class of materials. It is particularly challenging to study atomically thin metallic materials. To tackle this challenge, we have developed a new thermal conductivity measurement method based on the temperature dependent electrical resistance change and analyzed our method analytically and numerically by finite element method. We applied our method to 2H-TaS_2 and found thermal conductivity as 9.55±1.27 W/m.K. Thermal conductivity value of TaS_2, a metallic transition metal dichalcogenide was measured for the first time. This is supported by Wiedemann-Franz law and thermal conductivity of similar materials such as 2H-$TaSe_2$ and 1T-TaS_2. The method can be applied to semiconducting thin materials as well and is superior to other methods in various ways.

Keywords: thermal conductivity, 2D materials, temperature dependent resistance change, finite element method, heat equation.

ÖZET

İKİ BOYUTLU MALZEMELERİN TERMAL İLETKENLİKLERİNİN ÖLÇÜMÜ İÇİN YENİ YÖNTEM

Onur Çakıroğlu
Fizik Bölümü, Yüksek Lisans
Tez Danışmanı: Talip Serkan Kasırga
Eylül 2019

Termal iletkenlik, malzemelerde ısı transferini belirleyen bir sabittir. Enerji üretim sistemindeki verimin ve mikro yapılarda soğutma mekanizmasının öneminin artmasından sonra, mikro ve nano malzemelerde termal iletkenliği bulmak için birçok ölçüm yöntemi ortaya çıkmıştır. Fakat, deney düzeneğinin kurulumundaki karmaşıklıklar, önerilen cihazların üretimindeki zorluklar ve ısı denklemlerinin direk çözümlerinin olmaması bir grup malzemeler için bu yöntemlerin kullanılamamasına neden olmaktadır. Özellikle atom kalınlığındaki metalik malzemeler üzerinde çalışmak zordur. Bu problemleri çözmek için sıcaklığa bağlı elektriksel direnç değişimine dayanan yeni bir ölçüm yöntemi geliştirdik ve yöntemimizi analitik ve sonlu elemanlar yöntemiyle sayısal olarak analiz ettik. Yöntemimizi 2H-TaS_2'a uyguladık ve ısı iletkenliğini 9.55±1.27 W/m.K olarak bulduk. TaS_2'ın, metalik bir geçiş metali dikalkogenit olan, termal iletkenliği ilk defa ölçülmüş oldu. Ölçümler Wiedemann-Franz kanunu ve 2H-$TaSe_2$ ve 1T-TaS_2 gibi benzer malzemelerin termal iletkenliği ile uyumlu bulundu. Yöntem, yarı iletken ince malzemelere de uygulanabilir ve çeşitli sebeplerle diğer yöntemlerden daha üstündür.

Anahtar sözcükler: ısıl iletkenlik, 2B malzemeler, sıcaklığa bağlı direnç değişimi, sonlu eleman metodu, ısı denklemi.

Acknowledgement

After 4 years physics education, I have dived into research. In the beginning, many frustrated experimental attempts, complicated papers and my own clumsiness have accompanied with me. Moreover, physics lectures have caused countless all day studies. Fortunately, I have been successful both in lectures and laboratory duties. However, I have recognized that these accomplishments have not been completely belong to myself so that there are some people which I have to present my gratefulness.

First, I would like to thank my advisor T. Serkan Kasırga to give me research opportunity by guiding in technical points and encouraging for studies in new fields. I am also glad to take advice and opinions from Engin Durgun, Bülent Ortaç and Seymur Jahangirov.

I would like to thank my lecturers Ahmet Gökalp and Ceyhun Bulutay for Quantum Mechanics, Cemal Yalabık for 6 major physics lectures and Salim Çıracı to teach Condensed Matter Physics which I have studied in this thesis. I can conveniently say that they have converted a simple child to an experienced and grown person since they have taught not only their lectures but also tips about life by giving many examples from their personal lives.

I would like to thank my friends Koray Yavuz, Enes Aybar, Efekan Kökcü, Muhammed Bilgin, Yağmur Aksu, Tuğba Andaç, Umutcan Güler, Engin Can Sürmeli, Gizem Akman, Müge Fidan, İzel Sarı and İhsan Demirel for their supports and motivations time to time. I would like to thank also SCM Lab members.

Education begins at home. My education journey started with my father Mustafa and my mother Fatma so I would like to thank them for their support and motivation. I would like to thank my little brother Ozan due to his friendly suggestions and sarcastic replies. And my lovely wife, Merve... I couldn't imagine this process without her support, motivation speeches and kindness. I would like to thank her for these.

Finally, I would like to extend my thanks and acknowledgement to Türkiye Bilimsel ve Teknolojik Araştırma Kurumu (TÜBİTAK) for funding this work under the grant numbers 118F061 and 214M109.

Contents

List of Figures

List of Tables

Chapter 1

Introduction

1.1 Motivation

Discovery of new materials opened a window to the solutions of some engineering problems, new applications for the daily life, and improvement of existing devices by features which were non-existent before. Thermal properties of materials is fascinating and thermal applications can be evaluated in two important titles; heat dissipation and thermoelectric generators as shown in Figure 1.1.

Efficient heat dissipation is most common and desired application nowadays because of decreased performance of CPUs and GPUs in computers or cellphones under heavy heat load, while massive heat flows from electric stove to pots is a necessary feature in modern kitchens. Thermoelectric generators is much more related to efficiency of applications. Car engines convert almost 25% of fuel energy to mechanical energy and the remaining energy is converted to the heat. Thermoelectric generators move electrons by temperature gradient and convert thermal energy to electrical energy literally. If system equations are considered, thermal conductivity (κ is symbol in equations and TC as an abbreviation will be used in this thesis for it) takes a most important role in these applications as shown in Equation 1.1 and this makes studies of thermal conductivity essential.

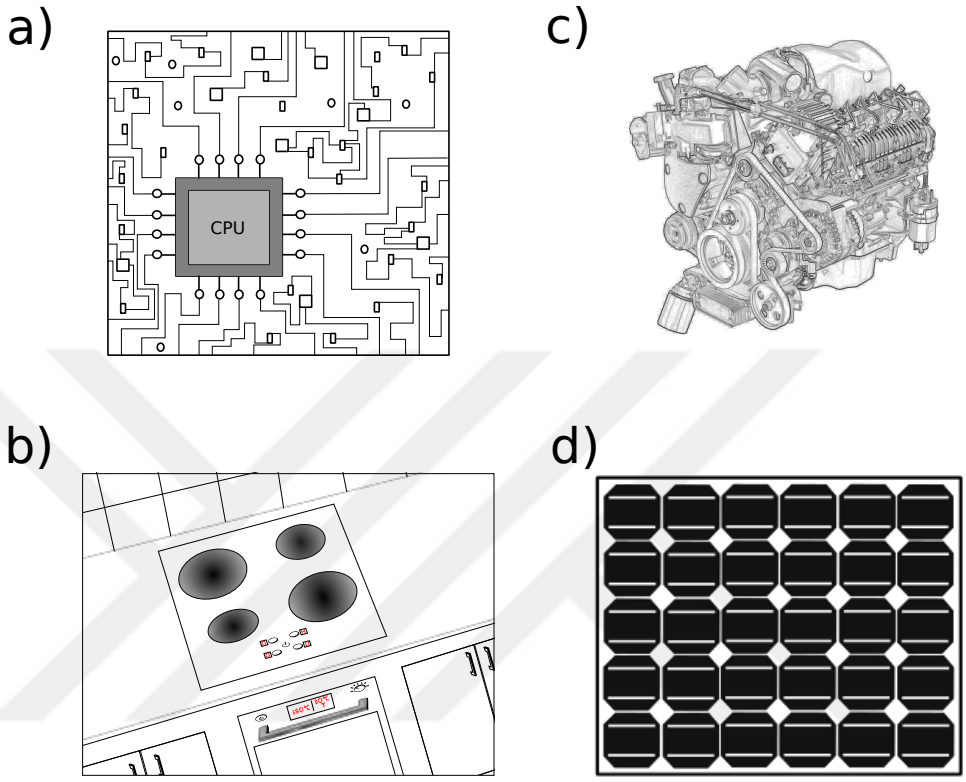

Figure 1.1: Some Applications of Thermal Properties of Materials. All of them are related to thermal conductivity (κ) values of materials. **a-b** are examples of heat dissipation and **c-d** are thermoelectric generators. **a)** computer CPU as a cooling application **b)** electric stove as a heating application **c)** car engine as an application which converts wasted heat to electrical energy [1] **d)** solar cell as a system in which increasing of efficiency should be necessary.

$$Q = \kappa.\Delta T \qquad and \qquad ZT = \frac{S\sigma^2}{\kappa}T \tag{1.1}$$

Q, T, ΔT, S and σ are heat per unit volume, temperature, temperature change, Seebeck coefficient and electrical conductivity respectively. First equation is known as Fourier's law and shows conduction of heat in materials. Other is thermoelectric figure of merit (ZT) and determines the maximum efficiency of a thermoelectric material. [2]

Moreover, one of the major research subjects in scientific area is two dimensional materials since 2004.[10] Most common studies exist on graphene,

hBN (hexagonal boron nitride), MoS_2 (molybdenum disulfide) and bP (black phosporous). Their structures consist of mainly layers and they are stacked together by van der Vaals interaction (non-van der Vaals bond plays a role in stacking was shown newly also [11]). Their fascinating properties make it possible to study new research areas like valleytronics [12, 13], spintronics [14, 15, 16], quantum dots[17] and topological insulators [18]. Thermal conductivity of 2D materials is also explained in this research field. Extreme values for TC can be found such as 5300 W/m.K [3] in graphene and 0.23 W/mK in SnSe [19]. Therefore, 2D materials allow working over a wide range of thermal conductivity. Materials having high thermal conductivity values can be used in the heat dissipation application while ones having low TC values can be implemented into thermoelectric generators.

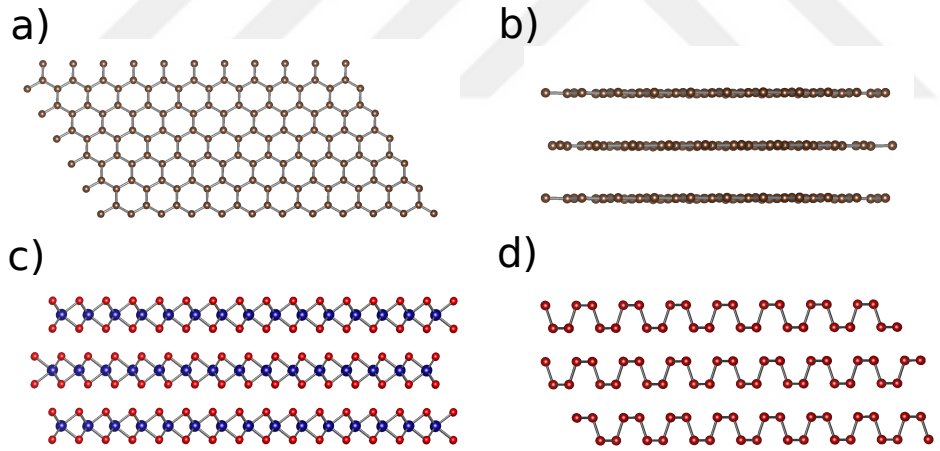

Figure 1.2: Representation of 2D Materials at Different Views **a)** and **b)** are top and side views of hexagonal structures as demonstration of graphene or hBN. **c)**side of view for MoS_2 and **d)** for bP.

Measuring thermal conductivity of 2D materials becomes essential since their TC values are different than the values of their 3D counterparts. There are many methods (as explained in next section) to measure TC. These methods are used to measure common materials like graphene or MoS_2. Due to the complexity of the methods or their being not capable to measure other 2D materials, especially the metallic ones so a new method is needed.

Recently, we performed scanning photocurrent microscopy(SPCM) measurements on NbS_2 to find the local photoresponse on metallic 2D materials at zero and finite bias. Although photothermal effect is not expected in metallic materials due to high TC values and low photon absorption in the visible range, NbS_2 crystals show photocurrent generation can be possible by local heating by the laser excitation. [20] However, TC value of 2D NbS_2 crystals is not known accurately in the monolayer limit as TC values for many other 2D materials and previous methods used are not proper for the measurement. Therefore, we worked on developing a new method and we believe that it can fill this measurement gap.

1.2 Overview of Thermal Conductivity

1.2.1 Heat Transfer and Thermal Conductivity

Heat transfer is defined as an energy movement from one place to another. Heat flows via three modes; conductive, convective and radiative modes. Conductive mode is heat transfer through a material; for instance, a metal bar whose two ends are at different temperature carries heat conductively from hot zone to cold zone. Convective mode is heat transfer via a mass. In the winter, radiator using in order to get heated to room is a good example for this mode. Radiative mode is the result of blackbody radiation. Any material at a temperature radiates and causes energy (or heat) transfer. These three modes can exist at the same time but generally one of them dominates others. [2]

Moreover, thermal conductivity (TC) is related to conductive mode and an intrinsic property of material which determines how much heat flows through the materials.[21] Therefore, knowing TC values of materials helps to improve and develop heat applications. Furthermore, it is also temperature dependent so that knowing at which temperature of TC values are taken is also important. Temperature dependent TC values of some metals are shown in Figure 1.3 in order to gain familiarity to numerical TC values.

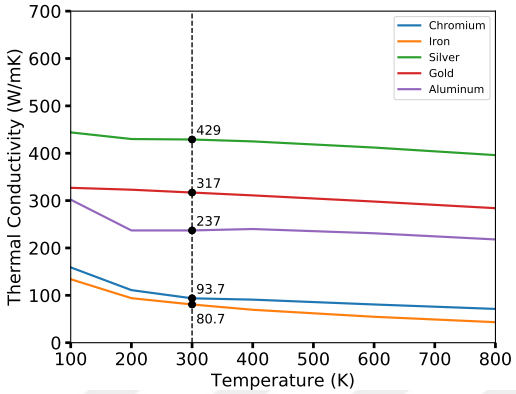

Figure 1.3: Thermal Conductivity Values of Some Metals and Their Temperature Dependence. Dash line shows room temperature and TC values at this point. [2]

In this thesis, conductive modes will be mainly focused for two dimensional materials at room temperature in the atmosphere environment while convective (especially air cooling) and radiative modes are neglected due to their minor contribution to their thermal properties and make analysis easier, as the common attitudes in measuring thermal conductivity in literature [22, 23].

1.2.2 Thermal Conductivity Measurement Techniques

There are many techniques to measure the thermal conductivity of solids but some of them will be mentioned to facilitate classification and present techniques easier. They can be categorized into steady-state and transient measurement techniques. First group requires a thermal stability to perform experiment after heating while second ones can be applied in a short time without waiting for steady-state condition. [24]

Before beginning to mention previous methods, it is better to discuss what the general measurement strategy is. Temperature dependent quantity has to be measured by changing temperature and then a relation between thermal conductivity and the quantity has to be set. In the following sections, the temperature

dependent quantities and their relations will be discussed. Advantages and disadvantages will be discussed as well. Finally, some TC values measured by the methods discussed will be given to familiarize the reader with TC values of 2D materials.

1.2.2.1 Steady State Techniques

a) Raman Scattering Based Method This technique allows researchers to measure thermal conductivity by dependence of Raman active modes to the temperature in Raman spectroscopy (which is obtained by differences between incident and scattering light from materials and can be defined as a material fingerprints) [25].

A laser is used to both heat the sample and perform Raman spectroscopy. 2D crystals are stayed on holes or trenches in the experiment since

- Heat can flow from the crystals to wafer and the measurement depends on not only thermal conductivity of materials but also TC of substrate and Thermal Boundary Conductivity (TBC) between substrate and the materials.
- The substrate absorbs and reflects laser beam so that temperature of the crystal can be changed by reflection from the substrate.

Laser beam is generally chosen with a Gaussian profile. It creates a temperature distribution on the crystal along radial direction and Raman signal belongs to part where temperature variation exists. Thus, an average temperature is assumed and analysis is made by this assumption.

Raman peak shift for TC was proposed and TC of graphene was measured by Balandin and his colleagues for the first time. [3] They have used G peak, which is characteristic peak of graphene in Raman spectroscopy. The peak location

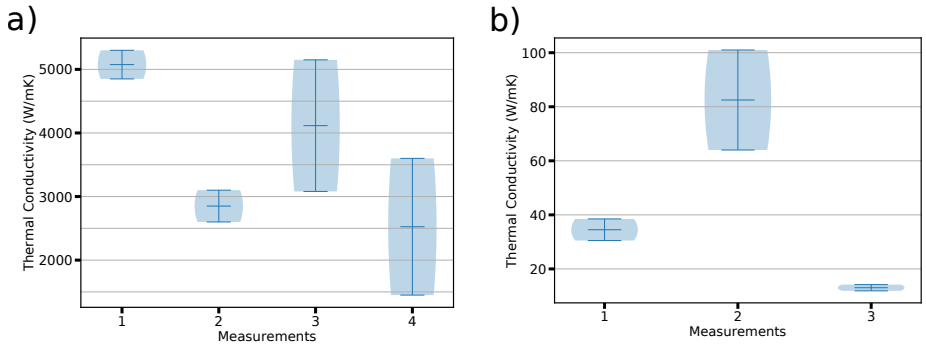

Figure 1.4: Thermal Conductivity Values from Literature **a)** TC for suspended monolayer graphene varies from 1450 to 5300 W/mK. Measurements were performed by Balandin and et. al. [3], Chen and et. al. [4], Ghosh and et. al. [5], Cai and et. al. [6] respectively. **b)** TC for suspended monolayer MoS_2 varies from 11.9 to 101 W/mK. Measurements were performed by Yan and et. al. [7], Zhang and et. al. [8], Bae and et. al. [9] respectively.

changes by temperature change so they set relation between Raman peak shift and thermal conductivity (κ) as

$$\kappa = \chi_G \left(\frac{L}{2hW}\right) \left(\frac{\delta\omega}{\delta P}\right)^{-1} \tag{1.2}$$

where χ_G is the slope of temperature dependence in peak shift vs power graph, L is half length of the suspended piece (material is transferred on a trench), h is thickness, W is width of crystal, $\delta\omega$ is peak shift and δP is change in heating power (Derivation of the relation can be found in Appendix A). As L, W and h are known, χ_G and ratio of $\delta\omega$ and δP can be obtained from the measurement, κ was subtracted easily by Equation 1.2 [3]

Figure 1.4 shows thermal conductivity values of monolayer graphene and MoS_2 obtained from literature. However, different research groups have found very different TC values for these materials by this method. Table 1.1 consists of some thermal conductivity values which belongs to some 2D materials also.

Major advantage of the Raman-based method is that the measurement is performed as non-contact. Therefore, the materials are not affected by fabrication of structures and the experiment can be done easier than the other methods.

Material	Number of Layer	TC Value (W/mK)	Ref
Graphene	Few Layer	1300-2800	Ref [23]
MoS_2	Few Layer	52	Ref [26]
WS_2	Monolayer/Bilayer	32/53	Ref [27]
hBN	Few Layer	227-280	Ref [28]
bP	Few Layer	10-40	Ref [29]

Table 1.1: In-plane Thermal Conductivity of Some Suspended Materials Measured by Micro-Raman Method At Room Temperature.

b) Micro-Thermometer Method This method is a miniaturization of thermal conductivity measurement in macro-systems via a thermometer and a heater. The system consists of a micro heater and a thermal sensor. Thermal sensor is a resistor whose temperature dependence is known. If the material is electrically conductive, an insulator layer is deposited in between the material and the contact in order to avoid short-circuit. In this method, researchers use two or four probes and calculations change depending on the number of probes. Basically, they heat the crystal from a contact, measure temperature from other in two probe system and use a heat transfer equation as shown in Equation 1.3

$$Q = \kappa.\nabla T \tag{1.3}$$

Two probe measurement uses the heat equation itself but there are four cases to be solved in four probe system since the heat is given from probes one by one and measure temperature from others so that there are four equations and their coupled solutions consist of 9 unknown parameters (including thermal boundary conductance between each contact and the material). Yet, only 3 of them are independent. One of these 3 parameters is thermal conductivity of the material. Table 1.2 shows some TC values obtained by micro-thermometer method.

Advantage of this technique is that the measurement concept is similar to its macroscopic counterpart. Therefore, modeling and configuring can be easier than other techniques since many of them are already done for measurement in the macro world.

Material	Number of Layer	TC Value (W/mK)	Ref
Graphene	Monolayer / Bilayer	600 / 490-700	Ref [30]/[31]
MoS_2	Few Layer	27-35	Ref [32]
hBN	Few Layer	250-360	Ref [33]
bP	Few Layer	49-81 (zz)/17-35(ac)	Ref [34]
WTe_2	Few Layer	~ 3	Ref [35]

Table 1.2: In-plane Thermal Conductivity of Some Materials Measured by Micro-Thermometer Method At Room Temperature. 'zz' and 'ac' represents TC values along zigzag and armchair direction.

1.2.2.2 Transient Techniques

a) TDTR and FDTR Time domain thermoreflectance method (TDTR) and frequency domain thermoreflectance method (FDTR) are based on temperature dependent reflectance. When a laser hits a material, the laser beam is reflected or absorbed by it. Reflection and transmission are intrinsic properties and can change with temperature. Therefore, one of them can be used as a quantity which help to deduce thermal conductivity value of material. Moreover, TDTR and FDTR are almost similar techniques except that TDTR uses a time delay between the pulse and the probe laser (as will be discussed) while the other method is based on varying frequency of the laser beam at a fixed time delay. TDTR will only be explained not to repeat many steps in their measurement techniques.

In TDTR, changing laser beam intensity is measured in time since the intensity is resulted by reflection from the materials. An ultrafast laser (typically Ti:sapphire laser) is used as a heat source in the optical circuit as shown in Figure 1.5. Laser beam is split into two parts, pump laser to heat sample and probe laser to measure the thermoreflectance (Two different laser sources are used in FDTR).[36] Generally, pulse laser beam reflected also from the sample is blocked physically to improve probe signal by separating two beams (so that they are 4 mm apart) and putting an obstacle (an iris) on the pulse path before the detector. Electro-optic modulator is to adjust the modulation frequency of laser beam and to use that frequency as reference point in lock-in amplifier to cancel any noise and signal except at that frequency. In this way, any sensitive changes can be

measured. Lock-in amplifier has two outputs; in-phase (V_{in}) and out-of-phase (V_{out}). Researchers take ratio of them to find thermal conductivity. Time delay between the probe and the pulse laser beams is utilized to avoid steady-state constraint so heat equation has a time term with specific heat and density of the materials. [37]

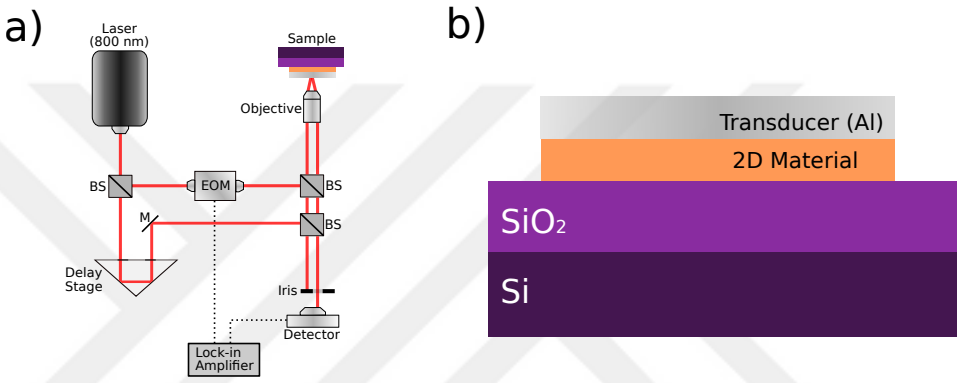

Figure 1.5: Demonstration of Setup and Sample in Time-Domain Thermoreflectance Method. **a)** Optic circuit schema. EOM, BS and M are electro-optic modulator, beam splitter and mirror respectively. Iris is to block pulse beam. **b)** Device schema. Thin film or 2D crystals are coated by a transducer in actual device to obtain linear behavior from the relation between temperature and reflectance and to increase signal strength.

In the analytical part, time dependent heat transfer equation in cylindrical coordinate is solved with frequency dependent Gaussian laser beam as shown in Equation 1.4 in order to obtain T(r, z, t). In the equation, C, ρ, κ_r and κ_z are specific heat capacity, density of material, TC in-plane and TC through plane respectively. Then, temperature change (ΔT) can be found theoretically. As the detector in the experiment measures the probe laser beam and its intensity change is caused by temperature change because of the pulse beam, relation between theoretical and experimental ΔT can be set. It is not possible to measure the ΔT directly but they use experimental data (V_{in}/V_{out}) and apply curve-fit to find many parameters with thermal conductivity. [38]

$$C\rho\frac{\partial T}{\partial t} = \kappa_r \frac{1}{r}\frac{\partial}{\partial r}\left(r\frac{\partial T}{\partial R}\right) + \kappa_z \frac{\partial^2 T}{\partial z^2} + \dot{Q}(r,\omega) \tag{1.4}$$

In the sample preparation, there is no need for a trench or a hole under the sample to remove effect of substrate like in micro-Raman method. However, every material has different thermoreflectance response so that a material, whose thermoreflectance response to temperature change is known and it is linear in a specific temperature range, should be chosen to perform the experiment. Therefore, a metal called transducer (generally Aluminum) is deposited on the material as shown in Figure 1.5-b. [39] This introduces more terms to be determined in the heat equation. These terms are obtained by a curve fit or used from literature. Moreover, thermal conductivity through plane (κ_z) is found first in general to increase accuracy of TC in-plane (κ_r) in the second measurement by increasing laser beam size and making heat equation one dimensional. [40] Some of the thermal conductivity values obtained by this method can be found in Table 1.3.

Advantage of this method is that fabrication is easier than other methods since there is no need to suspend the sample on a hole or a trench, no need to transfer crystal from one wafer to another and contacts are not necessary. Hence, fabrication steps are less and the measurement can be done after deposition of metal on the crystals as a transducer.

Material	**Number of Layer**	**TC Value (W/mK)**	**Ref**
Graphene	Bulk	1660-2140	Ref [41]
MoS_2	Few Layer	58-102	Ref [42]
WS_2	Few Layer	120	Ref [42]
hBN	Few Layer	263-367	Ref [41]
bP	Few Layer	62-86 (zz)/26-34 (ac)	Ref [43]
ReS_2	Few Layer	52-88 (zz)/37-63 (ac)	Ref [44]

Table 1.3: In-plane Thermal Conductivity of Some Supported Materials Measured by TDTR Method At Room Temperature. 'zz' and 'ac' represents TC values along zigzag and armchair direction.

b) 3ω Method This method is based on the frequency change of AC voltage due to a measured material while system is heated along a metal line on it by an AC current. Since source is AC and frequency dependent, temperature of sample is also varies with a frequency. Researchers set a relation between this frequency and TC so that they can find TC without need to steady state condition.[45] The

line between two contact is put on the sample and under the material. If the sample is conductive, an insulator is deposited on top of the sample. AC current passing through the line heats both the contacts and the sample. Temperature of line increases by a power like

$$P(t) = I^2 R_0 = \frac{1}{2} I_0^2 R_0 \left(1 + cos\left(2\omega t\right)\right) \tag{1.5}$$

where AC current(I) is $I_0.cos(\omega t)$. t and ω are time and frequency of AC current in the equation. Power has two component; time-dependent and independent and they can be called as AC and DC parts of power. Therefore, resistance change by power becomes

$$R(t) = R_0 \left(1 + \beta \Delta T_{DC} + \beta |\Delta T_{AC}| cos\left(2\omega t + \phi\right)\right) \tag{1.6}$$

where β is temperature coefficient, . Then, measurable voltage with AC current becomes

$$\begin{aligned} V = I.R = I_0 R_0 \Bigg[& \left(1 + \beta \Delta T_{DC}\right) cos(\omega t) + \frac{1}{2} \beta |\Delta T_{AC}| cos(\omega t + \phi) \\ & + \frac{1}{2} \beta |\Delta T_{AC}| cos(3\omega t + \phi) \Bigg] \end{aligned} \tag{1.7}$$

The method is called as 3ω due to last term in the equation and voltage measurement in 3ω frequency gives temperature oscillation. [46]

In the analysis part, solving a time-dependent heat transfer equation in semi-infinite cylindrical system for finite width of the heater is needed. [47] Then, it is possible to find thermal conductivity of the materials by the voltage.

Advantage of 3ω method is that a simple contact configuration is enough to perform the experiment. No need to hole or trench makes fabrication easier.

1.3 Challenges

Each method has advantages as already mentioned but they are not perfect. Their disadvantages make these methods inappropriate for some materials like

metallic TMDCs (TaS_2 or NbS_2) and the disadvantages will be discussed one by one in this section.

Raman based thermal conductivity measurement systems have limitations because of thermal sensitivity of measurements.[48] Therefore, these techniques should be modified in order to become major measurement technique in thermal conductivity but this might make analysis more difficult. For instance, Tianyu Wang and coworkers tried to eliminate the effect of laser power on Raman shift by using frequency-resolved Raman spectroscopy while measuring TC. However, their effort on analysis and experiment increased and they couldn't find TC value directly when they could be in ordinary micro-Raman method so that they used simulation software to find TC. [49] Moreover, every 2D materials does not have a Raman peak which is strong and has sensitive temperature response. Therefore, the method cannot be applied on every 2D crystal.

Micro-thermometer system can be easily fabricated for insulator material measurement but researchers have to deposit insulating layer between metallic/semiconducting materials and contacts. Therefore, fabrication and subtracting TC from heat equation becomes harder. Especially finding TC consists of more terms (like thermal boundary conductance) in the equation and this decreases accuracy because of assumptions or accepting more values from literature. Thus, such system is not proper for conductive materials.

TDTR methods have a complex analysis because of solution of time dependent heat transfer equation and increased number of parameters by using a transducer. These enforce researchers to make much more approximation even if solution of heat or diffusion equation with time dependence is not easy already. Moreover, scientists use some parameters from the literature to find TC value but this makes TC far from the correct value. Researchers who use equipment in optical setup, especially for ultrafast laser beam, have to have experience in optics. Therefore, the method is not for general use.

3ω method can be used especially for thin films but it is not suitable to measure TC value of many 2D crystals since the signal is not enough to detect even

by a lock-in amplifier system. Moreover, an insulator layer has to be deposited between material and contacts when measuring metallic materials so that fabrication becomes harder in this system.

As can be seen, a new technique is required for measurement of TC in order to improve accuracy of measurements, to apply to a wide range of materials and to make analysis easier in the solution of heat transfer equation. In the next chapters, such a new method will be discussed in detail, fabrication and analysis will be shown.

Chapter 2

Description of the Proposed Method

Thermal conductivity (TC) is not an independently measurable quantity like voltage or crystal thickness as mentioned previously. Therefore, a measurable quantity should be connected to thermal conductivity. This quantity is Raman shift in Raman-based system and changing thermoreflectance in TDTR by changing temperature of samples. Temperature dependent resistance is used as the measurable quantity in this new TC measurement method instead of Raman shift and thermoreflectance.

Every material is affected by temperature differences and some of their properties change depending on the changing temperature by flowing heat along them. Resistivity, one of such properties, of metallic and semiconducting materials has specific response to temperature change as shown in Equation 2.1 [50, 51, 52]

$$\begin{aligned} \rho &= \rho_0 \left(1 + \beta \left(T - T_a\right)\right) && \text{for metals} \\ \rho &= \rho_0 \exp\left(\frac{E_g}{2k_B T}\right) && \text{for semiconductors} \end{aligned} \tag{2.1}$$

Therefore, temperature effect on the resistivity can be used by measuring resistance of crystals. Relation between resistance(R) and TC value couldn't be set without flowing heat or creating a temperature gradient. If the heat transfer equation is written, the situation become more clear

$$\frac{\partial}{\partial x}\left(\kappa\frac{\partial T}{\partial x}\right)+\frac{\partial}{\partial y}\left(\kappa\frac{\partial T}{\partial y}\right)+\frac{\partial}{\partial z}\left(\kappa\frac{\partial T}{\partial z}\right)+\dot{Q}=C\rho_d\frac{\partial T}{\partial t} \tag{2.2}$$

where κ, $\dot{Q}$, C, ρ_d and t are thermal conductivity, heat source (per unit volume per unit time), specific heat, density of material and time variable.[53] Thus, if there is no temperature gradient or its changing in time, finding TC value is not possible. In the measurement, steady-state conditions are provided for simplicity. That's the system can reach equilibrium and temperature does not change anymore. Hence, time contribution in the Equation 2.2 can be canceled with specific heat and density of the material. Main formula for temperature distribution with a constant κ value (and for this thesis) becomes

$$\kappa\frac{\partial^2 T}{\partial x^2}+\kappa\frac{\partial^2 T}{\partial y^2}+\kappa\frac{\partial^2 T}{\partial z^2}+\dot{Q}=0 \tag{2.3}$$

Then, relation between R and TC can be set. If T in the Equation 2.3 is solved and the solution is put into any of Equation 2.1, a measurable quantity R (by converting ρ to R) becomes connected to TC and this shows that R can be used to deduce value of thermal conductivity. However, solution of heat transfer equation with temperature dependent resistance does not give κ value alone. Therefore, κ in obtained theoretical formula is adjusted until that model and experimental data match.

Until now, idea behind the new measurement method was described. It is better to discuss also fabrication or required device and the actual calculation of TC since there are some important points to be mentioned in the experimental and the analysis parts. A heat source is needed to create temperature gradient so a laser beam with a Gaussian profile is used. Many mechanisms emerge by laser excitation in 2D materials. Photovoltaic effect is generally considered in

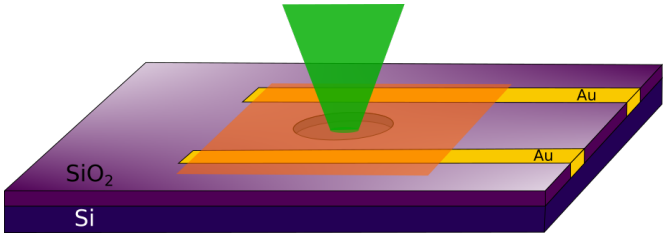

Figure 2.1: Illustration of the Measurement System. Orange color represents the 2D crystal. Green one is the laser beam. Hole is under it to prevent heating wafer by the laser. Au contacts are used to measure resistance.

semiconductors since laser can create electron-hole pairs that can be separated by built in electric fields. However, M. Buscema and his colleagues show that if energy of laser is less than band gap of the semiconductors or carrier diffusion length is short, photothermal effect plays major role.[54]

Thickness of 2D crystals measured in this thesis is in the nanometer scale so they are deposited on a suitable substrate. Si/SiO_2 wafer is chosen for that purpose. Substrate under the material removes a great portion of the heat deposited by the laser. If the laser beam is parked on the crystal, heat can flow through not only the crystal but also the wafer so thermal conductivity belongs to both of them. Therefore, a holes or trench should be drilled and the material should be transferred on them. A demonstration of the system with a hole can be seen in Figure 2.1

This configuration creates two solutions regions for the heat equation as suspended part of crystal is heated with a source but the supported part is cooled down by the wafer. A detail explanation will be given in Analysis chapter.

In the experiment, resistance with and without the laser should be measured to find TC value. Resistance differences (ΔR) between laser-on and off state can be related to TC and two probe method for measurement of resistance become applicable in the new measurement method. Although, measured R value consists of contact resistance (R_c) in two probe system, R_c in both laser-on and off state eliminates each other by subtracting R values as shown in Equation 2.4

$$\begin{aligned} \Delta R = R_{on} - R_{off} &= R_2 + R_c - R_1 - R_c \\ &= R_2 - R_1 \end{aligned} \tag{2.4}$$

where R_1 and R_2 are crystal resistances in laser-off and on state. Therefore, contact resistance in the experiment is not a problem in this experimental model.

Because a laser beam heats the material, temperature gradient exists along the material. Therefore, resistance change due to temperature is depending on distance to source center so local resistance change at each point has to be considered. For that purpose, temperature distribution has to be calculated first. There are two options; analytical calculation for a specific shape (for instance rectangular or square crystals) and finite element method (FEM) for any crystal shape.

In the thesis, temperature distribution is found by FEM and analytical calculations and they are used also to compare results. This is because, crystals are obtained by exfoliation and it gives random shaped crystals. Hence, there is no possibility to find an analytic solution for the crystals. Moreover, there are some methods to give a desired shape the crystals, such as Inductively Coupled Plasma and Focus Ion Beam, but they damage the crystals by creating defects on them and increase fabrication steps [55, 56].

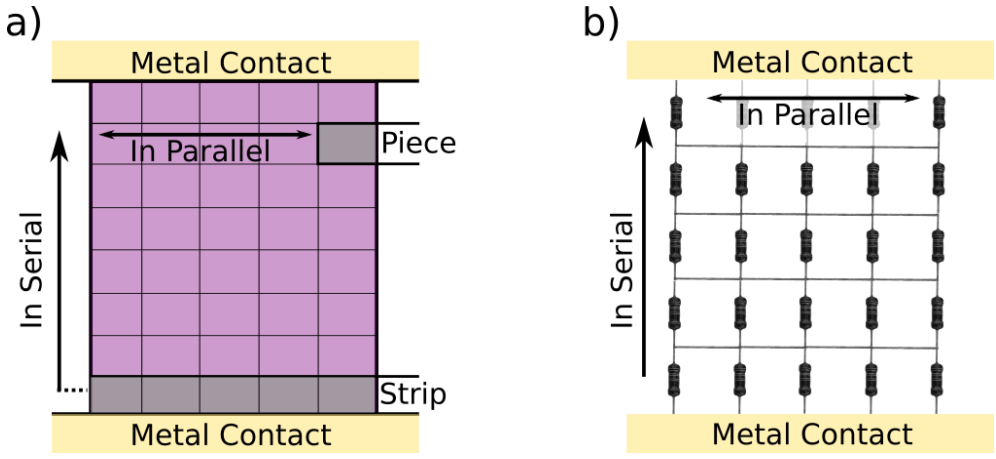

Figure 2.2: Calculation of Equivalent Resistance **a)** Calculation strategy in real crsytal is to split it into strips and pieces and then collect in serial and in parallel. **b)** Demonstration of resistance calculation in an electrical circuit.

Resistance should be calculated for each local temperature point due to non-homogeneous temperature distribution. Therefore, the crystal is split into strips from one contact to another and strips are split into pieces to find equivalent resistance. Resistance of pieces in each strips are summed in parallel and then strips are added in series as a typical electrical circuit. Figure 2.2 shows this similarity.

Analysis by FEM simulation or analytic solution is needed to fit a TC value in order to find temperature distribution. The strategy is to pick a TC value, analyze by these methods and find a ΔR. If ΔR is not equal to experimental one, repeat the same procedure until finding same ΔR in experiment and in the analysis. TC value, which gives to this final ΔR, becomes actual thermal conductivity of the crystal.

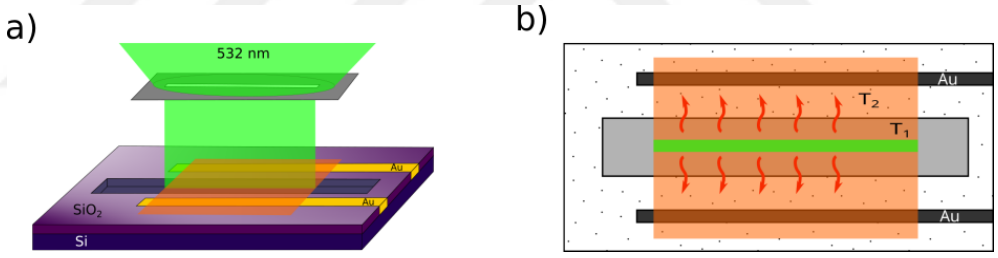

Figure 2.3: Thermal Conductivity Measurement by Trench System **a)** An apparatus is used to obtain a homogeneous source from a Gaussion beam laser and it shines through the crystal suspended on the trench. **b)** This homogeneous beam and trench configuration makes heat transfer equation a 1D problem.

Although some crystals have isotropic thermal conductivity through in-plane like graphene and MoS_2, another crystals can behave differently in x and y axis. Both cases should be carefully evaluated. Circle shape has symmetry in radial direction so holes under the suspended part of crystal can be used only in isotropic TC. However, trench along a crystal can be proper in anistropic TC. If the Gaussian laser beam is cut almost from its full width half maximum, laser beam turns into a homogeneous heat source. Then, the beam shines along the material on the trench heats the sample only through one-direction as shown in Figure 2.3 and makes possible to measure thermal conductivity along x and y axis separately only by performing the experiments in both armchair and zigzag direction of the crystals.

In the next chapters, the fabrication steps will be discussed in the detail and then how to find temperature distribution by simulation will be mentioned with the analytical solution of heat transfer equation in different cases.

Chapter 3

Device Fabrication

Fabrication of the devices alters the pristine qualities of the 2D materials due to chemicals involved in the process; therefore, it should be mentioned in order to give some clues about these standard fabrication steps and clarify their roles in measurements. It consists of two main techniques; top contact and bottom contact. We employed both techniques since they have some advantages and disadvantages. However, we have encountered serious problems in top contact fabrication so measured devices are produced by bottom contact technique as will be explained.

3.1 Top Contacted Devices

In this method, main purpose is to avoid largely possible interface problem between contacts and crystal in any electronic measurements. In our case, this is not a problem since ΔR is used in the analysis and effect of contact resistance is eliminated. However, this contact type is preferred mostly in the literature [57, 58] so we optimized the fabrication of the top contact device first. Fabrication steps are shown in Figure 3.1.

First step is to drill holes on wafer. A laser is used as a heater and it can

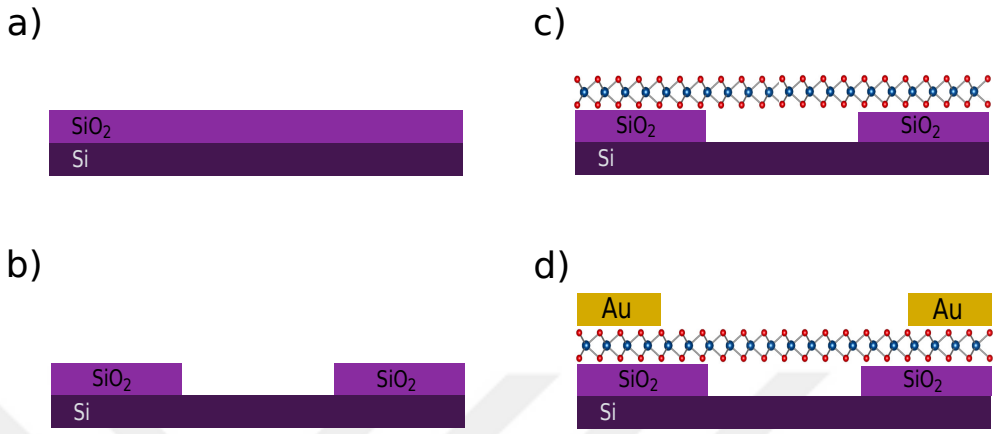

Figure 3.1: Fabrication steps of top contact devices **a)** Pristine Si/SiO_2 wafer with 1000 nm oxide layer **b)** Drilling hole to prevent the heat flow to SiO_2 while heating crystal at the center of hole by laser **c)** Crsytal transfer by CAB film **d)** Putting gold contacts by coating PMMA, giving custumized shapes to PMMA by EBL and deposited gold by E-Beam evaporator

increase temperature of wafer also without holes. In that case, analysis of thermal conductivity only for crystal becomes wrong since heat flows through both wafer and the crystal so that thermal conductivity value belongs to wafer and crystal coupled system. To avoid such a scenario, holes were drilled on wafers. Their radii should be large enough such that temperature in the borders of holes must be ambient temperature with laser-on state. Obviously, the radii should be larger than radius of laser beam also. After consideration of general thermal conductivity values of TMDCs and the radius of laser beam ($\sim$1 μm), the radii were decided as larger than 1 μm.

We tested several methods to obtained holes. First we tried Buffered Oxide Etch (BOE) on Electron Beam Lithography (EBL) patterned samples. Desired holes were drawn in KLayout program. 1000 nm Si/SiO_2 wafer was coated by 495 PMMA A6 polymer before EBL with a standard spinner recipe (1000 rpm for 5 sec, 3000 rpm for 40 sec with 1000 rpm/sec for both steps).Then coated wafer was patterned by EBL for holes on wafer and patterned parts of polymer were removed by developer. Wafer were ready to etch after EBL patterning and parts of wafer under removed parts of polymer were etched by BOE for 10 minutes to obtain 750 nm depth. It is an isotropic etchant so edges of holes become not

vertical but rounded as shown in Figure 3.2.

In the crystal transfer, we have used polycarbonate (PC) as carrier since 2D material are so thin and transfer can be performed by only such carrier. [59] First, crystals are exfoliated on an empty wafer, and then this wafer is coated by PC via spinner after determining a suitable crystal in microscope for TC measurement. Then, the crystal is transferred on a targeted hole by moving PC via microcontroller in microscope. Wafer is heated to dry PC and it is dissolved in chloroform so that the crystal stays on the wafer without any polymer on it. However, the crystals teared on the holes when crystals were transferred. Possible explanation for tearing was that crystal might bend on holes too much due to rounded edge so that it is teared and it looks like we need vertical walls by anisotropic etch.

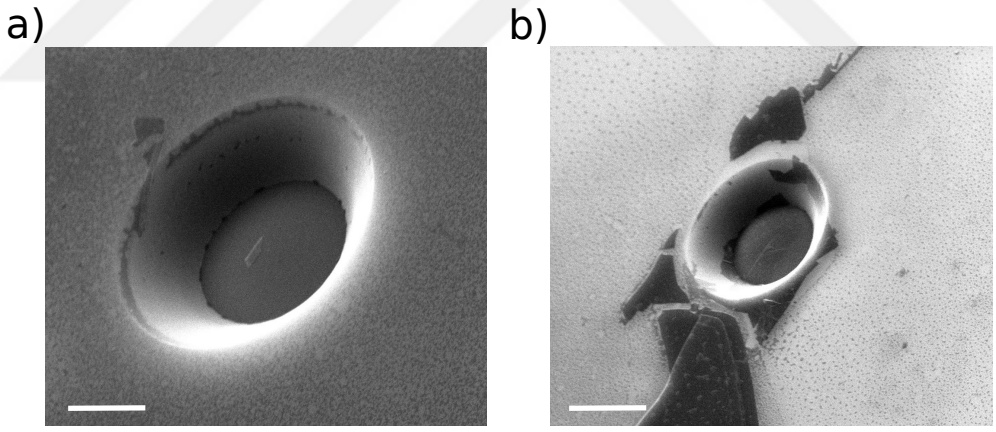

Figure 3.2: SEM image of a hole and a transferred crystal on it **a)** An etched wafer by buffered oxide etchant (BOE) after EBL process **b)** Failure of crystal transfer on hole made by BOE. Scale bars are 2 μm.

Therefore, we have changed the etching technique and use Inductively Coupled Plasma (ICP), which etches wafer by plasma of some aggressive gases, since it can etch Si anisotropically and we thought that it can etch SiO_2 similarly. However, we couldn't obtain vertical walls by anisotropic etching in ICP since we couldn't stop in-plane etch too much. After many trials, we have resulted in holes shown in Figure 3.3. It looks like the hole etched by BOE in Figure 3.2-a except a little anisotropy. Moreover, we couldn't use Si as wafer since it is conductive and causes short circuit in electrical measurements.

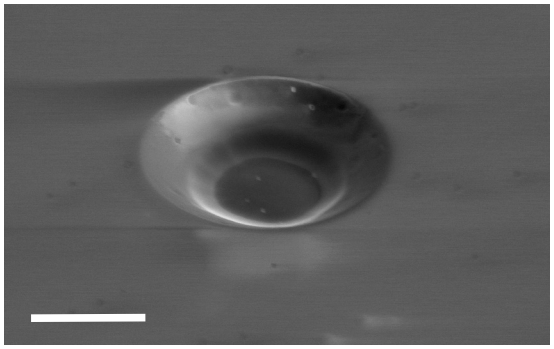

Figure 3.3: SEM image of a hole etched by ICP. 13.56 MHz coil and 396 KHz plate were set to 250 W and 30 W respectively and CH_3F and 0_2 gasses were given at 100 and 30 sccm rate. ICP chamber was worked at 25 °C for 12 min. Scale bar is 3 μm.

We have been suspicious about transfer method and lithography step. Crystals were damaged in transfer step due to the side of wall and similarly it can be damaged also in lithography step even if they would be survive in the transfer. This is because chemical compounds Polymethyl methacrylate (PMMA) for lithography and a developer after lithography are used. Hence, these treatments would cause crystals damaging also. Therefore, we have changed fabrication technique without performing next steps as shown in Figure3.1-c and d so produced all devices by bottom contact method.

3.2 Bottom Contacted Devices

In this method, the main purpose is to preserve the crystals from harm caused by fabrication processes since they are not on wafer through whole fabrication process. Fabrication consists of three steps as shown in Figure 3.4.

We have added a more important step to the method. Common attitude for bottom contact fabrication is to deposit metal contact on top of the wafer after lithography step. However, this creates a stress on crystal since there is a height difference between contact and wafer so the material takes a shape of this step-like structure. Moreover, this can change thermal conductivity by changing thermal

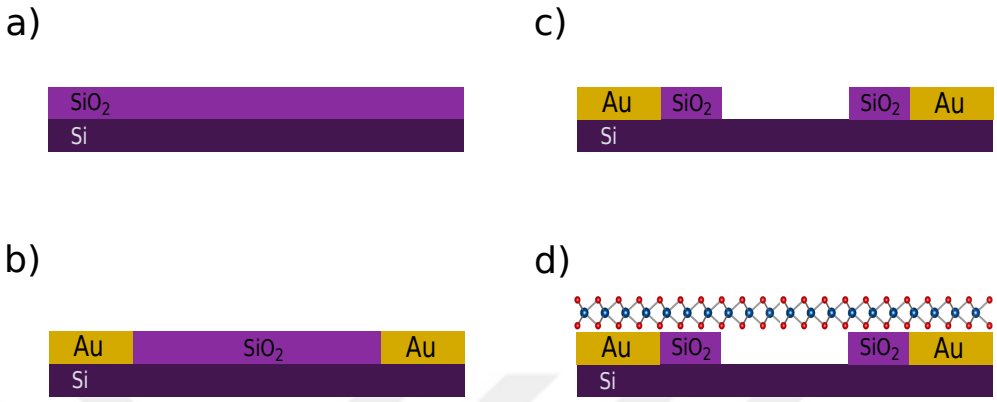

Figure 3.4: Fabrication steps of bottom contact devices **a)** Pristine Si/SiO_2 wafer with 1000 nm oxide layer **b)** Depositing gold contacts after optic lithography and etching as much as contact height. **c)** Drilling hole by FIB to prevent the heat flow to SiO_2 while heating crystal at the center of hole by laser **d)** Crsytal transfer.

transport through material. Therefore, we etch contact area first and then fill the gap by gold as shown in Figure 3.4-b. Furthermore, atomic force microscopy (AFM) proves that height levels of metal contact and wafer are same in Figure 3.5

Drilling holes on wafer was improved also. Focus Ion Beam (FIB) was used to obtain vertical walls as desired in top contact. It was applicable for top contact devices but possible damage in lithography led us using bottom contact devices as mentioned previously. In FIB, Ga ion hits the wafer vertically and removes atoms from the surface so vertical wall can be achievable. Hence, we have drilled wafer and obtained such holes as shown in Figure 3.6.

In the transfer steps, we have tried three methods. Firstly, polycarbonate (PC) was used as transfer film as in top contact fabrication. However, the crystals couldn't survive in this transfer method. Secondly, we have tried to coat by Cellulose Acetate Butyrate (CAB) which is another polymer to use in crystal transfer. Same procedures are followed again but CAB is dissolved in ethyl acetate this time. Unfortunately, many trials have ended failures except few cases and survive ones have been so thick. One of failures by CAB is shown in Figure 3.7

We have passed to another method. This method is called as dry method

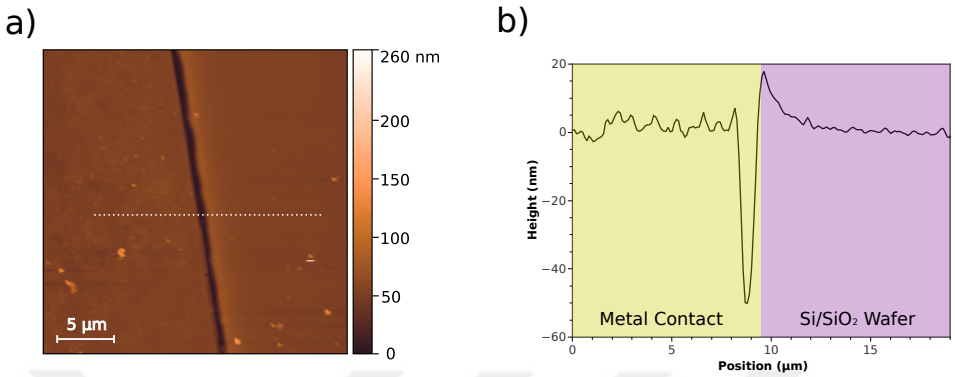

Figure 3.5: AFM Result of Device After Etch and Gold Evaporation **a)** AFM scanning was taken from separation between metal contact and Si/SiO_2 wafer. Dash line shows place in which height profile is obtained. **b)** Height profile shows clearly that there is no height differences between contact and wafer.

and Polydimethylsiloxane (PDMS) is used as carrier. However, wafers are not coated by PDMS. It is prepared before transfer and exfoliation is performed on PDMS. Then, a crystal is selected in microscope and transfer on holes is done by adjusting with help of micro-manipulator. After heat treatment at 85 °C, PDMS and wafer are separated gently. Crystals are attached to wafer instead of PDMS due to adhesiveness. Figure 3.8 shows one of successful crystal transfers. Samples are ready for TC measurement after such a device can be prepared.

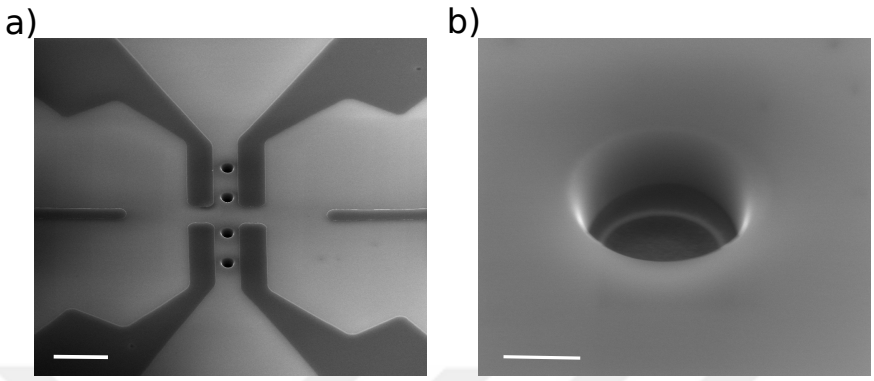

Figure 3.6: Drilling Holes by FIB. **a)** Hole configuration in bottom contact after optical lithography, ICP and gold evaporation is shown. Contact configuration is used for many purpose in lab such as measurement of hall effect so it is not prepared for TC measurement specifically and two of six contacts are eliminated since they are not applicable for this project. **b)** Image of a hole in SEM demonstrates that FIB drills until Si layer of Si/SiO_2 wafer. Thickness of SiO_2 in the wafer is 1000 nm so desired depth is achieved. Scale bars are 10 and 1 μm respectively.

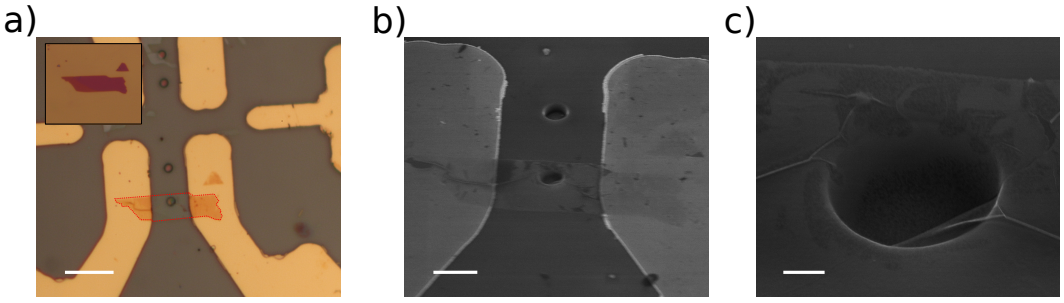

Figure 3.7: Crystal Transfer Failure by CAB **a)** The image shows an almost prepared TC device. The crystal is MoS_2 and red dash line is to make crystal edge more prominent. contrast demonstrates that crystal is few layered. Inset image is an exfoliated MoS_2 before transfer. Scale bar is 15 μm. **b)** SEM image was taken after transfer to find whether the crystal is survive or not. Red dash line shows crystal edge also. Scale bar is 5 μm. **c)** SEM image clarifies that the crystal was ripped. Scale bar is 0.5 μm.

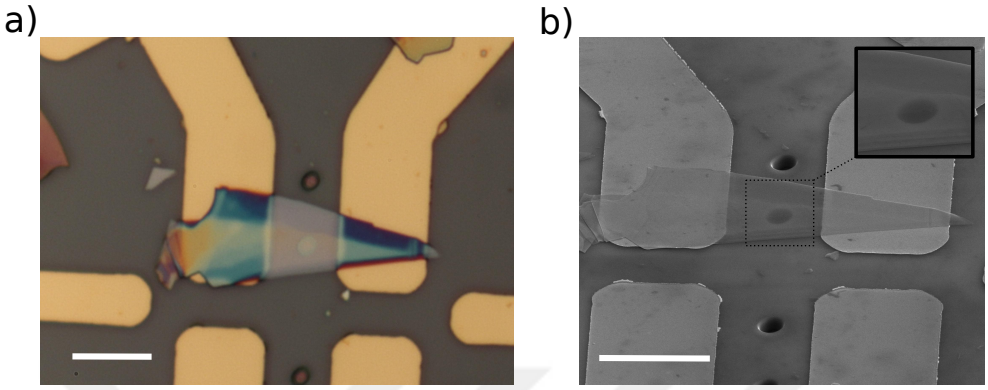

Figure 3.8: Successful Crystal Transfer **a)** Optical image shows that crystal stays on the hole and metal contact clearly. Color differences of crystal are caused by background color since crystal is thin and it is transparent at a ratio. **b)** SEM image demonstrates that crystal is not damaged on hole. Scale bars are 10 μm

Chapter 4

Analysis

Some of crystal properties are related to thermal conductivity (TC) and the value is detected from this relation. As mentioned before, it is related to changing Raman shift in micro-Raman method or related to changing reflectance of material surface in time-domain thermoreflectance (TDTR).

The method in this thesis makes thermal conductivity related to changing resistance by heat. However, some consideration is needed first. Center of laser beam has the highest temperature as the laser spot has a Gaussian profile. Therefore, temperature distribution should be found since temperature of each location on the crystal is different. Then, total changing resistance is calculated by temperature distribution since it is already known relation. For instance, resistivity of metals changes like

$$\rho = \rho_0 \left[1 + \beta(T - T_a)\right]$$

Resistivity of each point can be found and equivalent resistance can be extracted by serial and parallel connection. Moreover, there are two types of thermal conductivity; isotropic and anisotropic TC. If the crystal has same quantity at different orientation, it is called as isotropic. However, quantity might be orientation dependent, that's TC through x-axis and TC through y-axis might be different. Then it is called anisotropic.

Therefore, at least two relations have to be set. Strategy is to find the temperature distribution by the analytical solution in isotropic and anisotropic crystals separately with different experimental setup configuration. Furthermore, air effect and radiation in both cases will be neglected. Then, finite element method will be introduced since geometric constraints in the analytic solution can be eliminated by the simulation.

4.1 Determination of Temperature Distribution Analytically

4.1.1 Analytical Solution For Isotropic Materials

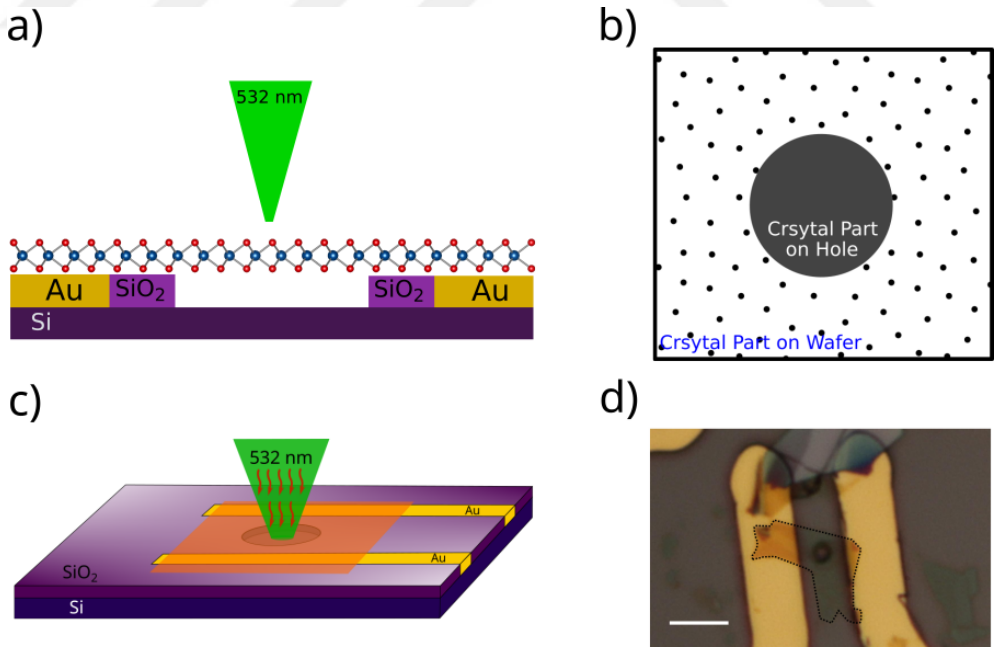

Figure 4.1: Device demonstrations and its image **a)**Side view of bottom contact device **b)**3D demonstration of the device **c)**Top view of the device to show analytic solution regions. Black circle is suspended crystal part and represents temperature distribution of Equation 4.1. Dotted region is supported part and represents of Equation 4.2. **d)** Real image of the device. Black dash line shows the crystal edges. Scale bar is 5 μm.

Crystal is transfered on a hole as shown in Figure 4.1. A laser shines on the center of the hole to become a heat source. Vacuum environment, Gaussian laser beam and steady-state heat flow are assumed to solve the heat equation and wafer (SiO_2) behaves like a heat sink in the system. There are two general formula because of two different areas of the crystal; for suspended part (piece on hole) and supported part (piece on substrate) of crystal and these are; [6, 60, 7]

$$\kappa \frac{1}{r}\frac{d}{dr}\left[r\frac{dT_1(r)}{dr}\right] + q(r) = 0 \qquad and \qquad q(r) = \frac{I\alpha}{t}\ \exp\left(-\frac{r^2}{r_0^2}\right) \qquad r < R \ \ (4.1)$$

and

$$\kappa' \frac{1}{r}\frac{d}{dr}\left[r\frac{dT_2(r)}{dr}\right] - \frac{G}{t}\left[T_2(r) - T_0\right] = 0 \qquad r > R \ \ (4.2)$$

where $\mathbf{R}$ is hole radius, $\boldsymbol{\kappa}$ and $\boldsymbol{\kappa'}$ are thermal conductivity of suspended and supported 2D material (for simplicity, relation between them is accepted as linear $\epsilon\kappa = \kappa'$) , $\mathbf{T_1(r)}$ and $\mathbf{T_2(r)}$ are temperatures in suspended and supported areas, $\mathbf{q(r)}$ is volumetric Gaussian beam heat, $\mathbf{r_0}$ is the Gaussian beam radius, $\mathbf{I}$ is laser power per unit area ($P/\pi r_0^2$), $\boldsymbol{\alpha}$ is absorbance of crystal, $\mathbf{t}$ is thickness of the crystal, $\mathbf{G}$ is thermal transmittance and $\mathbf{T_0}$ is ambient temperature. General solutions of equation 4.1 and 4.2 are;

$$T_1(r) = c_1 + c_2 \ln(r) + \frac{a r_0^2}{4\kappa}\mathrm{Ei}\left(-\frac{r^2}{r_0^2}\right) \qquad where \qquad a = \frac{\alpha I}{t} \qquad r < R \ \ (4.3)$$

$$T_2(\gamma) = c_3 I_0(\gamma) + c_4 K_0(\gamma) + T_0 \qquad where \qquad \gamma = r\left[\frac{G}{\kappa' t}\right]^{1/2} \qquad r > R \ \ (4.4)$$

where I_0 and K_0 are zero order modified bessel function of first and second kind. Ei is not a elementary function and it is called as exponential integral. If we consider boundary conditions, they are

(i) $\quad T_2(r \to \infty) = T_0$

(ii) $\quad \left.\frac{dT_1(r)}{dr}\right|_{r\to 0} = 0$

$$\text{(iii)} \qquad -\kappa \left.\frac{dT_1(r)}{dr}\right|_{r\to R} = -\kappa' \left.\frac{dT_2(\gamma)}{dr}\right|_{r\to R}$$

$$\text{(iv)} \qquad \left.T_1(r)\right|_{r\to R} = \left.T_2(\gamma)\right|_{r\to R}$$

First and second boundary conditions suggest that $T_2(r)$ and $T_1(r)$ should be finite when r$\to \infty$ and r$\to$0 respectively, therefore derivative of T_1 should be zero and T_2 become equal to room temperature. Third and last boundary conditions imply continuity of heat flow at the boundaries. Using these conditions, we need to find coefficients. If first boundary condition is used, we get;

$$\boxed{c_3 = 0}$$

since $I_0(\gamma)$ goes to infinity as r goes to infinity. Second boundary condition gives;

$$\frac{dT_1(r)}{dr} = \frac{c_2}{r} + \frac{ar_0^2}{4\kappa}\,\frac{2e^{-\frac{r^2}{r_0^2}}}{r} = 0$$

$$\left[\frac{c_2}{\not{r}} + \frac{ar_0^2}{2\kappa\not{r}}e^{-\frac{r^2}{r_0^2}}\right]_{r\to 0} = 0$$

$$\boxed{c_2 = -\frac{ar_0^2}{2\kappa}}$$

If we use third boundary condition;

$$\kappa\left[\frac{c_2}{R} + \frac{ar_0^2}{2\kappa}\,\frac{e^{-\frac{r^2}{r_0^2}}}{R}\right] = -\kappa'\left[c_4 K_1(\gamma_{_R})\sqrt{\frac{G}{\kappa' t}}\right]$$

$$\frac{ar_0^2}{2R}\left[1 - e^{-\frac{R^2}{r_0^2}}\right] = c_4 K_1(\gamma_{_R})\sqrt{\frac{G\kappa'}{t}}$$

$$\boxed{c_4 = \frac{ar_0^2}{2RK_1(\gamma_{_R})}\sqrt{\frac{t}{G\kappa'}}\left[1 - e^{-\frac{R^2}{r_0^2}}\right]}$$

and fourth boundary condition gives

$$c_1 + c_2 ln(R) + \frac{ar_0^2}{4\kappa}\mathrm{Ei}\left(-\frac{R^2}{r_0^2}\right) = c_4 K_0(\gamma_{_R}) + T_0$$

$$c_1 = T_0 + c_4 K_0(\gamma_R) - c_2 ln(R) - \frac{a r_0^2}{4\kappa} \mathrm{Ei}\left(-\frac{R^2}{r_0^2}\right) \tag{4.5}$$

where γ_R is $R\sqrt{\frac{G}{\kappa' t}}$. If we substitute c_2, c_4 and put **I** into c_4, equation 4.5 becomes

$$\boxed{c_1 = T_0 + \frac{\alpha P K_0(\gamma_R)}{2\pi R t K_1(\gamma_R)} \sqrt{\frac{t}{G\kappa'}} \left[1 - e^{-\frac{R^2}{r_0^2}}\right] + \frac{\alpha P}{4\pi t \kappa} \left[2\ln(R) - \mathrm{Ei}\left(-\frac{R^2}{r_0^2}\right)\right]}$$

If we use Equation 4.3 and 4.4 to see temperature distribution of system by inserting coefficients, it becomes as shown in Figure 4.2.

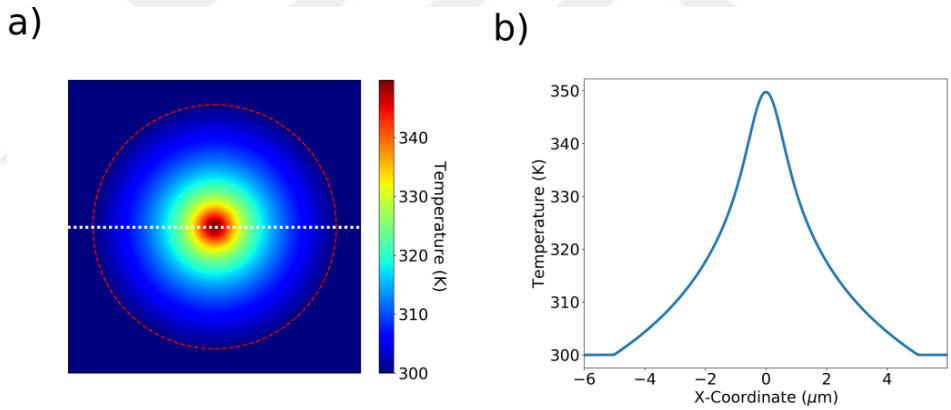

Figure 4.2: Results of Solution of Heat Equations for Isotropic Measurement. **a)** Demonstration of Temperature Distribution. Red dash circle shows boundary of hole on which crystal is suspended. Hole radius (R) is 5 μm, thickness of crystal (t) is 0.65 nm, thermal conductivity of suspended crystal (κ) is 34.5 W/mK, ratio of thermal conductivity of supported to suspended ones (ξ) is 0.9, half of the Gaussian beam width (r_0) is 0.5 μm, laser power is 0.1 mW, absorbance (α) is 2.7%, thermal transmittance (G) is 50 MW/m^{2}K and ambient temperature (T_0) is 300 K.**b)** Temperature Profile. It is obtained through white dash line in **a**.

4.1.2 Analytical Solution For Anistropic Materials

Modifying the method should be needed in order to measure anisotropic thermal conductivity (κ) through crystal inplane. Gaussian beam laser heats the crystal

circularly. Therefore, heat flows through radial direction as shown in Figure 4.3-a. If the Gaussian beam laser is applied for anisotropic crystals, κ value becomes average of κ values of distinct directions. Therefore, we have to change laser beam type for the anisotropy in such a way that temperature gradient is one dimensional. Z. Luo and his colleagues have proposed using an apparatus [61] to dissipate heats through only one direction as represented in Figure 4.3-b and c.

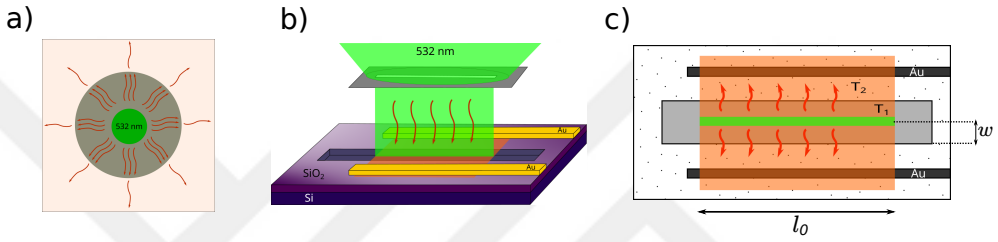

Figure 4.3: Radial heat flow and device representation of anisotropic thermal conductivity measurement system **a)** Heat flows equally if the crystal is isotropic through inplane according to thermal conductivity and Gaussian beam hits the center of the crystal. **b)** 3D representation of bottom contact device with the apparatus **c)** Top view of bottom contact device. h and l_0 are half width of trench and length of crystal respectively

Vacuum environment, 1D Gaussian beam laser and steady-state heat flow are assumed for solution of heat equation. Two heat equations for suspended and supported parts are

$$\kappa \frac{d^2T_1(x)}{dx^2} + q(x) = 0 \qquad where \qquad q(x) = \frac{I\alpha}{t} \exp\left(-\frac{x^2}{w_0^2}\right) \qquad x < w \quad (4.6)$$

$$\kappa' \frac{d^2T_2(x)}{dx^2} - \frac{G}{t}(T_2(x) - T_0) = 0 \qquad x > w \quad (4.7)$$

where $\mathbf{w}$ is half width of trench, $\boldsymbol{\kappa}$ and $\boldsymbol{\kappa'}$ are thermal conductivity of suspended and supported parts of the crystal, $\mathbf{T_1(r)}$ and $\mathbf{T_2(r)}$ are temperatures in suspended and supported areas, $\mathbf{q(x)}$ is heat source, $\mathbf{w_0}$ is full width half maximum of Gaussian beam, $\mathbf{I}$ is laser power per unit area ($P/\pi w_0^2$), $\boldsymbol{\alpha}$ is absorbance of crystal, $\mathbf{t}$ is thickness of the crystal, $\mathbf{G}$ is thermal transmittance and $\mathbf{T_0}$ is ambient temperature. General solutions of equation 4.6 and 4.7 are;

$$T_1(x) = C_1 + C_2 x - \frac{a\sqrt{\pi} w_0}{2\kappa} \left(\exp\left(-\frac{x^2}{w_0^2}\right) \frac{w_0}{\sqrt{\pi}} + \mathrm{erf}(\frac{x}{w_0})x \right) \qquad (4.8)$$

$$T_2(x) = T_0 + C_3 \exp\left(x\sqrt{\frac{G}{t\kappa'}}\right) + C_4 \exp\left(-x\sqrt{\frac{G}{t\kappa'}}\right) \tag{4.9}$$

where erf is error function. If we consider boundary conditions in order to find C_1,C_2,C_3 and C_4 they are

(i) $T_2(x \to \infty) = T_0$

(ii) $\left.\frac{dT_1(x)}{dx}\right|_{x\to 0} = 0$

(iii) $\left.-\kappa \frac{dT_1(x)}{dx}\right|_{x\to w} = \left.-\kappa' \frac{dT_2(x)}{dx}\right|_{x\to w}$

(iv) $\left.T_1(x)\right|_{x\to w} = \left.T_2(x)\right|_{x\to w}$

First and second boundary conditions suggest that $T_2(x)$ and $T_1(x)$ should be finite when $x\to \infty$ and $x\to 0$ respectively. Third and last boundary conditions imply continuity of heat flow at the boundaries. Using these conditions, we can find unknown coefficients. If first boundary condition is used, we get;

$$\boxed{C_3 = 0} \tag{4.10}$$

since second term in right side of equation 4.9 goes to infinity as x goes to infinity. Second boundary condition gives;

$$\left.\frac{dT_1(x)}{dx}\right|_{x\to 0} = C_2 - \frac{a\sqrt{\pi}w_0}{2\kappa}\left(\cancel{-\frac{2x}{w_0\sqrt{\pi}}\exp\left(-\frac{x^2}{w_0^2}\right)} + \operatorname{erf}\left(\frac{x}{w_0}\right) \cancel{+\frac{2x}{w_0\sqrt{\pi}}\exp\left(-\frac{x^2}{w_0^2}\right)}\right)\Bigg|_{x\to 0} = 0$$

$$\left.\frac{dT_1(x)}{dx}\right|_{x\to 0} = C_2 - \frac{a\sqrt{\pi}w_0}{2\kappa}\left(\cancel{\operatorname{erf}\left(\frac{x}{w_0}\right)}\right)\Bigg|_{x\to 0} = 0$$

$$\boxed{C_2 = 0} \tag{4.11}$$

If we use third boundary condition;

$$-\cancel{\kappa}\frac{a\sqrt{\pi}w_0}{2\cancel{\kappa}}\text{erf}\left(\frac{w}{w_0}\right) = -\kappa' C_4\sqrt{\frac{G}{t\kappa'}}\exp\left(-\sqrt{\frac{G}{t\kappa'}}w\right)$$

$$\boxed{C_4 = \frac{aw_0}{2}\sqrt{\frac{t\pi}{G\kappa'}}\frac{\text{erf}\left(\frac{w}{w_0}\right)}{\exp\left(-w\sqrt{\frac{G}{t\kappa'}}\right)}} \tag{4.12}$$

and fourth boundary condition gives

$$C_1 - \frac{a\sqrt{\pi}w_0}{2\kappa}\left(\exp\left(-\frac{w^2}{w_0^2}\right)\frac{w_0}{\sqrt{\pi}} + \text{erf}(\frac{w}{w_0})w\right) = T_0 + C_4\exp\left(-w\sqrt{\frac{G}{t\kappa'}}\right)$$

$$\boxed{C_1 = T_0 + C_4\exp\left(-w\sqrt{\frac{G}{t\kappa'}}\right) + \frac{a\sqrt{\pi}w_0}{2\kappa}\left(\exp\left(-\frac{w^2}{w_0^2}\right)\frac{w_0}{\sqrt{\pi}} + \text{erf}(\frac{w}{w_0})w\right)} \tag{4.13}$$

If we use Equation 4.6 and 4.7 to see temperature distribution of system by inserting coefficients, it becomes as shown in Figure 4.4.

4.2 Determination of Temperature Distribution by FEM

Analytic solution of heat transfer equation exists only for specific shapes (rectangle, cylinder or etc.) due to differential equation. However, exfoliated crystals have random shapes and there is no solution for this random geometries analytically. We have to apply a numerical method. There are finite difference method or finite integration method but well known and most common one of numerical methods for random geometries is Finite Element Method(FEM).

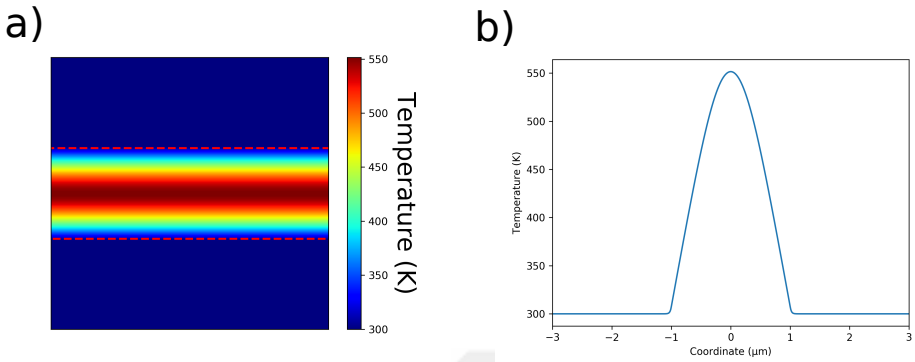

Figure 4.4: Results of Solution of Heat Equations for Anisotropic Measurement **a)** Demonstration of Temperature Distribution. Red dash line shows boundary of hole on which crystal is suspended. Trench size (2w) is 2 μm, crystal length and width (l_0) are 6 μm, thickness of crystal (t) is 0.65 nm, thermal conductivity of suspended crystal (κ) is 34.5 W/mK, ratio of thermal conductivity of supported to suspended ones (ξ) is 0.9, half of the Gaussian beam width (r_0) is 0.5 μm, laser power is 0.5 mW, absorbance (α) is 2.7%, thermal transmittance (G) is 50 MW/m^{2}K and ambient temperature (T_0) is 300 K.**b)** Temperature Profile. It is obtained from a line through vertical direction in **a**.

Temperature distribution for three different cases will be found in next three subsections. Although, FEM for the isotropic measurement will be discussed in first part again, some concepts of FEM will also mention first to be more clear. Then, anisotropic measurement will be covered.

4.2.1 FEM For Isotropic Materials

Finite element method can be easily explained by that all domain is divided by small pieces, in which an approximation function is assigned and connected to domain, and a solution of differential equation as number is found by boundary condition. However, it is needed more and systematic explanation to understand mechanism of FEM. Four steps can be defined [62];

- Mesh Domain to Create Subdomains
- Assign An Approximation Function to Subdomains by Mesh Shape

- Assembling all subdomains in the domain
- Solving the equation of system

Although whole domain doesn't give a solution in a complex shape, small specific shapes can give by good approximation and all subdomains can be assembled to obtain total results. There are many shapes for subdomains in 2D FEM simulation like triangular, rectangular or quadrilateral. Triangular shape will be focused in remaining part of the thesis.

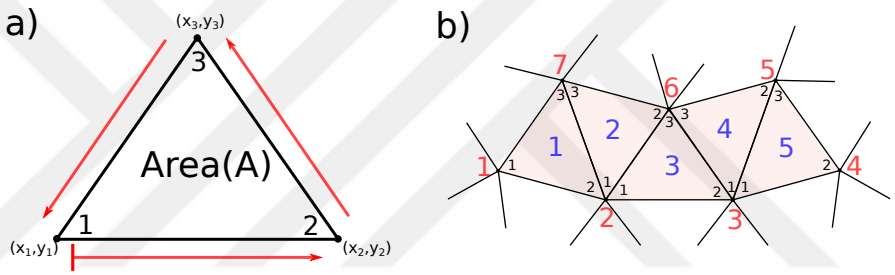

Figure 4.5: Demostration of Triangular Mesh Algorithm by MeshPy. **a)** It assigns numbers to the corners of triangles counterclockwise in each triangle. **b)** It assigns numbers to each corner and each triangle globally for assemble step. Black, blue and red numbers show corner number in a triangle, triangle number in domain and corner number in domain respectively. Three assigned numbers and each coordinates are stored as lists separately and produced by MeshPy as output of a function automatically.

First, we have to divide our system into subdomains and we need some extra operations to solve the equation of system. Each corner of triangle should be labeled by number to add effect of each point to triangle. Moreover, numbers should also be assigned to triangle to distinguish each one and connect them to total region. In this way, points contribute to triangles, triangles contribute to global or solution region. An open source python library (MeshPy) is used to mesh whole solution region by triangles and it deals with these labeling problems by distinguish outer points to apply boundary condition as shown in Figure 4.5. Another essential thing for FEM simulation is to link two regions of crystals, part on hole and part on substrate; however, the library links two region but does not distinguish their points and triangles. The source code of MeshPy was modified

and it can separate two regions according to points and triangles. A result of crystal mesh after applying MeshPy library to the crystal is shown in Figure 4.6.

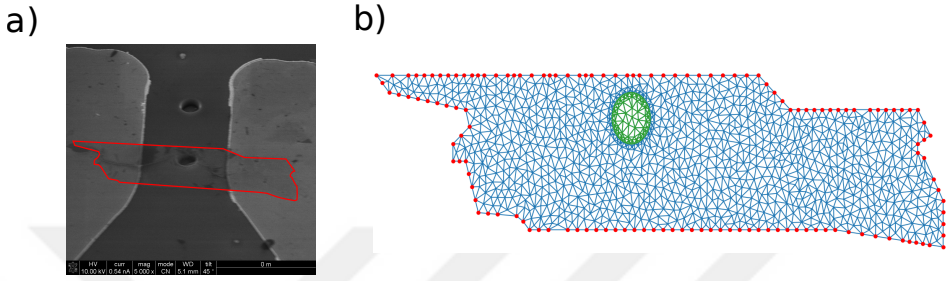

Figure 4.6: Mesh A Transfered Crystal by MeshPy **a)** Red line shows transfered crystal boundary on bottom contact devices **b)** Result is obtained by MeshPy. Green area shows pieces of crystal on hole while blue area represents pieces on substrate.

Next step is to determine approximation function. It is decided by what kind of shape used in mesh system is and the function gives a solution for subdomain approximately. The shape, we use in the thesis, is triangle and the linear approximation function for triangle can be written as [62, 63];

$$T(x, y) = a + bx + cy \tag{4.14}$$

The function can be written in higher orders like quadratic or cubic orders as written in Equations 4.15 and 4.16 (where a,b,c,d,e are coefficient and x,y are coordinate variables) but this makes calculation for the equation of system harder in the next steps. Therefore, linear form is preferred.

$$T(x, y) = a + bx^2 + cy^2 + dxy \qquad Quadratic\ Form \tag{4.15}$$

$$T(x, y) = a + bx^3 + cx^2y + dxy^2 + ey^3 \qquad Cubic\ Form \tag{4.16}$$

So far nothing has been done about the heat flow equation but they were all related to geometry or structure. Relation between structure and the equation is constructed by energy term. In order to calculate temperature distribution numerically, energy functional of system instead of Equation 4.1 on suspended part of crystal can be written as;

$$W' = \frac{1}{2} \iint_S \left[\kappa \nabla T^2 - 2Q.T\right] dS \tag{4.17}$$

and on supported part instead of Equation 4.2 as;

$$W'' = \frac{1}{2}\iint_S \left[\kappa \nabla T^2 - \frac{G}{t}(T - T_a)^2\right] dS \tag{4.18}$$

W′ and T′ in Equation 4.17 represents energy functional and temperature for suspended part while W″ and T″ in Equation 4.18 are for supported part.[64] κ, Q, G, t and T_a are thermal conductivity, heat source, thermal boundary conductance, thickness of crystal and ambient temperature respectively. Energy functional is used to apply calculus of variation for heat flow equation and minimized equation is found in this way to get a solution from complex geometrical system. [63]

Therefore, third step in FEM simulation begins with these energy functional. Before beginning, terms in the functional have to be changed since each term should be redefined in each subdomain. Thus, general formulas become

$$W'_e = \frac{1}{2}\iint_S \left[\kappa \nabla T_e^2 - 2Q_e.T_e\right] dS \tag{4.19}$$

and on supported part as [64];

$$W''_e = \frac{1}{2}\iint_S \left[\kappa \nabla T_e^2 - \frac{G}{t}(T_e - T_{ae})^2\right] dS \tag{4.20}$$

Each triangle in domain is called as element in FEM terminologically. Therefore, subscript 'e' in W_e, T_e, Q_e and $T_{a,e}$ represents elements in domain since every elements is connected to domain one by one in next step. In addition to redefining of functional, unknown coefficients in determined approximation function have to be determined and then elements can link to domain. Approximation function can be written in elements as

$$T_{e,i} = a + bx_i + cy_i \tag{4.21}$$

where subscript e and i are for an element (or a triangle) in domain and one of three points in this element. If Equation 4.21 can be written in matrix form in

an element,

$$\begin{bmatrix} T_{e,1} \\ T_{e,2} \\ T_{e,3} \end{bmatrix} = \begin{bmatrix} 1 & x_1 & y_1 \\ 1 & x_2 & y_2 \\ 1 & x_3 & y_3 \end{bmatrix} \begin{bmatrix} a \\ b \\ c \end{bmatrix} \tag{4.22}$$

If first matrix in right side is made inverse and put to left side, unknown values of a,b and c can be found. These values are substituted into Equation 4.21 for each point in the element and total temperature relation in the element can be written as

$$T_e = \sum_{i=1}^{3} \alpha_i(x, y) T_{e,i} \tag{4.23}$$

where

$$\alpha_1 = \frac{1}{2A}[(x_2y_3 - x_3y_2) + (y_2 - y_3)x + (x_3 - x_2)y]$$
$$\alpha_2 = \frac{1}{2A}[(x_3y_1 - x_1y_3) + (y_3 - y_1)x + (x_1 - x_3)y]$$
$$\alpha_3 = \frac{1}{2A}[(x_1y_2 - x_2y_1) + (y_1 - y_2)x + (x_2 - x_1)y]$$

A is defined as area of each triangle (or element) in domain and can be found by

$$A = \frac{1}{2}[(x_2 - x_1)(y_3 - y_1) - (x_3 - x_1)(y_2 - y_1)] \tag{4.25}$$

We have to find also Q_e and $T_{a,e}$ like T_e. Their approximation function also similar to T_e ($Q=a_Q+b_Q x+c_Q y$ and $T_a=a_{T_a}+b_{T_a} x+c_{T_a} y$) so that their total functions for an element from points become

$$Q_e = \sum_{i=1}^{3} \alpha_i(x, y) Q_{e,i} \tag{4.26a}$$

$$T_{ae} = \sum_{i=1}^{3} \alpha_i(x, y) T_{ae,i} \tag{4.26b}$$

Terms in energy functional were calculated for each elements until now so Equation 4.23 and Equation 4.26 can be inserted into Equation 4.19 and Equation 4.20 and the functionals become;

$$W'_e = \frac{1}{2}\sum_{i=1}^{3}\sum_{j=1}^{3}\kappa T_{e,i}\left[\iint_S \nabla\alpha_i\nabla\alpha_j dS\right]T_{e,j} - \sum_{i=1}^{3}\sum_{j=1}^{3}T_{e,i}\left[\iint_S \alpha_i\alpha_j dS\right]Q_{e,j} \tag{4.27}$$

and

$$W''_e = \frac{1}{2}\sum_{i=1}^{3}\sum_{j=1}^{3}\left\{\kappa T_{e,i}\left[\iint_S \nabla\alpha_i\nabla\alpha_j dS\right]T_{e,j} + \frac{G}{t}T_{e,i}\left[\iint_S \alpha_i\alpha_j dS\right]T_{e,j}\right. \\ -2\frac{G}{t}T_{e,i}\left[\iint_S \alpha_i\alpha_j dS\right]T_{ae,j} \\ \left.\frac{G}{t}T_{ae,i}\left[\iint_S dS\right]T_{ae,j}\right\} \tag{4.28}$$

The integrals can be defined as

$$C^e_{ij} = \iint_S \nabla\alpha_i\nabla\alpha_j dS \quad \textit{and} \quad D^e_{ij} = \iint_S \alpha_i\alpha_j dS \tag{4.29}$$

In this way, Equation 4.27 and Equation 4.28 can be written, to help write code especially, in matrix form as

$$W'_e = \frac{1}{2}\kappa[T_e]^t[C^e][T_e] - [T_e]^t[D^e][Q_e] \tag{4.30a}$$

$$W''_e = \frac{1}{2}\kappa[T_e]^t[C^e][T_e] + \frac{G}{2t}[T_e]^t[D^e][T_e] - \frac{G}{t}[T_e]^t[D^e][T_{ae}] + \frac{G}{2t}[T_{ae}]^t[D^e][T_{ae}] \tag{4.30b}$$

If what have been done so far are summarized, the domain was meshed, approximation function in subdomain was determined by meshing geometry, the energy functionals were written for two heat flow equations in order to determine governed equations in FEM simulation by minimum energy principles and total approximation functions in elements were substituted into the funtionals. Therefore, first two steps and half of third step mentioned in beginning of section were done. Remaining part is so crucial to write code and to figure out operation of FEM simulation. Relations in Equation 4.29 will be determined for elements first and then they will be assembled in domain (or all solution area). C^e_{ij}, (and similarly D^e_{ij},) can be written in matrix as[62]

$$[C^e] = \begin{bmatrix} C^e_{11} & C^e_{12} & C^e_{13} \\ C^e_{21} & C^e_{22} & C^e_{23} \\ C^e_{31} & C^e_{32} & C^e_{33} \end{bmatrix}$$

and each term can be calculated by each triangle (or element). For instance, C_{23}^e is calculated as

$$\begin{aligned} C_{23}^e &= \iint_S \nabla\alpha_2 \nabla\alpha_3 dS \\ &= \frac{1}{4A^2}[(y_3 - y_1)(y_1 - y_2) + (x_1 - x_3)(x_2 - x_1)] \iint_S dS \\ &= \frac{1}{4A}[(y_3 - y_1)(y_1 - y_2) + (x_1 - x_3)(x_2 - x_1)] \end{aligned}$$

or C_{22} as

$$\begin{aligned} C_{22}^e &= \iint_S \nabla\alpha_2 \nabla\alpha_2 dS \\ &= \frac{1}{4A^2}[(y_3 - y_1)^2 + (x_3 - x_1)^2] \iint_S dS \\ &= \frac{1}{4A}[(y_3 - y_1)^2 + (x_3 - x_1)^2] \end{aligned}$$

Therefore, C_{ij}^e can be generalized as

$$C_{ij}^e = \frac{1}{4A}\left(P_i P_j + Q_i Q_j\right) \tag{4.31}$$

if P and Q are defined as [62]

$$P_i = (y_j - y_k)\,,\ Q_i = (x_k - x_j) \tag{4.32}$$

The number i,j and k is determined by an order in Equation 4.32. If i is 1, j and k become 2 and 3. If i is 3, j and k become 1 and 2 respectively. This generalization helps to calculate C_{ij} matrix easily in code. Finding a generalized expression for D_{ij}^e is not easy so it is better to give expression directly [62]

$$D_{ij}^e = \begin{cases} A/12, & i \neq j \\ A/6, & i = j \end{cases} \tag{4.33}$$

All mesh pieces can now be put together. Assembling is done by corner number in domain and other assigned numbers help to determine links between corners. Two triangles in a domain will be used, as shown in Figure 4.7, to facilitate

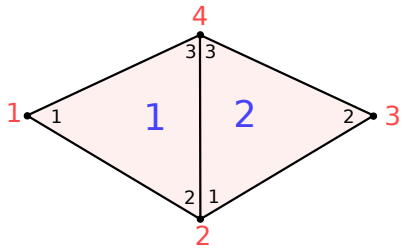

Figure 4.7: Example of A Simple Domain which Consists of Two Triangle. Black, blue and red numbers show corner number in a triangle, triangle number in domain and corner number in domain respectively.

explaining and understanding assemble. [C] matrix can be written as

$$[C] = \begin{bmatrix} C_{11} & C_{12} & C_{13} & C_{14} \\ C_{21} & C_{22} & C_{23} & C_{24} \\ C_{31} & C_{32} & C_{33} & C_{34} \\ C_{41} & C_{42} & C_{43} & C_{44} \end{bmatrix}$$

and each C_{ij} can be found by link between i and j corner in domain. For instance, C_{24} represents a link between 2 and 4 in domain (red numbers). C_{42} represents also same link so they must have a same value. Moreover, link consists of corner 2-3 in first triangle and corner 1-3 in second triangle (black number). C^1_{23} and C^2_{13} are found in triangle 1 and 2 (superscript shows triangle number in domain) by Equation 4.31 and C_{24} (and C_{42}) can be found as

$$C_{24} = C_{42} = C^1_{23} + C^2_{13}$$

C_{11} and C_{44} represent corner 1 (not a link) of first triangle and third corner of both triangles. Therefore,they can be found as

$$C_{11} = C^1_{11}, \quad C_{44} = C^1_{33} + C^2_{33}$$

However, there is no connection between corner 1 and corner 3 in domain (red numbers) so

$$C_{13} = C_{31} = 0$$

Remaining parts is found as below

$$C_{12} = C_{21} = C^1_{12}, \quad C_{32} = C^2_{12}, \quad C_{33} = C^2_{22}$$
$$C_{22} = C^1_{22} + C^2_{11}, \quad C_{41} = C^1_{13}, \quad C_{43} = C^2_{23}$$

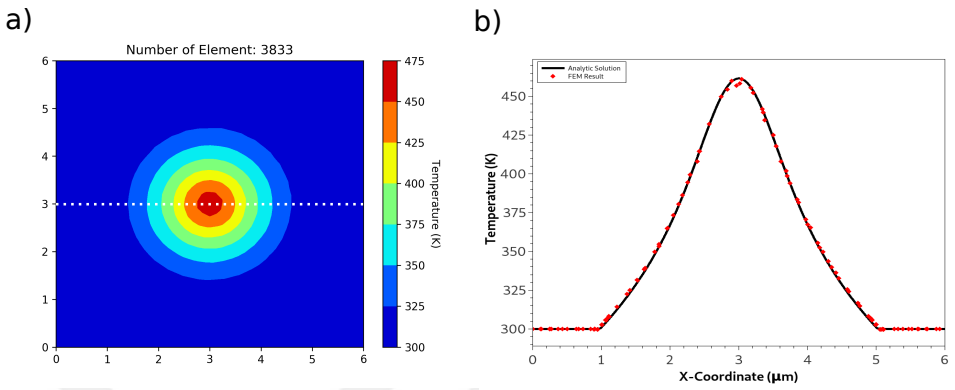

Figure 4.8: FEM Results for Isotropic Measurement **a)**Temperature distribution of FEM result. Parameters of simulation and analytic results are as follows; radius of hole is 2 μm thickness of crystal (t) is 0.65 nm, thermal conductivity of suspended crystal (κ) is 34.5 W/mK, ratio of thermal conductivity of supported to suspended ones (ξ) is 0.9, half of the Gaussian beam width (r_0) is 0.5 μm, laser power is 0.5 mW, absorbance (α) is 2.7%, thermal transmittance (G) is 50 MW/m^{2}K and ambient temperature (T_0) is 300 K. **b)** Comparison of Analytical Solution and FEM Result. Temperature profiles are obtained by data through white dash line in **a**.

Last duty in FEM is to solve general functions in Equation 4.27 and 4.28 and find a temperature expression (T_e) for each triangle corner. If energy functionals are minimized by considering calculus of variation, T_e can be found. First finding expression for T_1 and generalizing the results makes the calculation easier. Therefore, minimized energy functional in suspended part for T_1 is

$$\frac{\partial W}{\partial T_1} = \frac{\partial}{\partial T_1}\left(\sum_{e=1}^{n} W^e\right) = \frac{\partial W^1}{\partial T_1} = \frac{\partial}{\partial T_1}\left[\kappa\left(T_1C_{11}T_1 + T_1C_{12}T_2 + T_1C_{13}T_3 + T_1C_{14}T_4\right) - \left(T_1D_{11}Q_1 + T_1D_{12}Q_2 + T_1D_{13}Q_3 + T_1D_{14}Q_4 + T_2D_{21}Q_1....\right)\right] = 0$$

and this gives

$$T_1 = -\frac{1}{C_{kk}}\left(C_{12}T_2 + C_{13}T_3 + C_{14}T_4\right) + \frac{1}{\kappa C_{11}}\left(D_{11}Q_1 + D_{12}Q_2 + D_{13}Q_3 + D_{14}Q_4\right)$$

so if it is generalized, solution of T for suspended part becomes

$$\boxed{T_k = -\frac{1}{C_{kk}}\sum_{i=1,i\neq k}^{n} T_iC_{ki} + \frac{1}{\kappa C_{kk}}\sum_{i=1}^{n} Q_iD_{ki}} \tag{4.34}$$

In the same way, T in supported part by Equation 4.28 becomes

$$\boxed{T_k = -\frac{1}{C_{kk} + \frac{G}{t\kappa'} D_{kk}} \sum_{i=1, i\neq k}^{n} C_{ik} T_i - \frac{1}{\frac{t\kappa'}{G} C_{kk} + D_{kk}} \sum_{i=1, i\neq k}^{n} D_{ik} T_i + \frac{1}{\frac{t\kappa'}{G} C_{kk} + D_{kk}} \sum_{i=1}^{n} D_{ik} T_{a,i}} \tag{4.35}$$

If we use same parameters which are used in analytic analysis with same crystal structures and assume laser beam is Gaussian shape and parked in the center of suspended part of crystal (or on the center of hole) again, FEM gives result as similar as what analytic solution gives as shown in Figure 4.8.

4.2.2 FEM For Anisotropic Materials

So far, suspended part of the crystal stays on a predrilled circular hole in FEM calculations. However, the crystal is on a trench in the anisotropic measurements. Although analytic problem is different for isotropic and anisotropic cases, same energy functional in Equation 4.18 and 4.17 can be used in FEM calculation in anistropic situation. Only change exists in source formula. Radial direction was used for Gaussian beam but x (y) direction for vertical (horizontal) trench is used here since problem converts a 1D problem. After implementing new source into FEM equation, simulation results become as shown in Figure 4.9

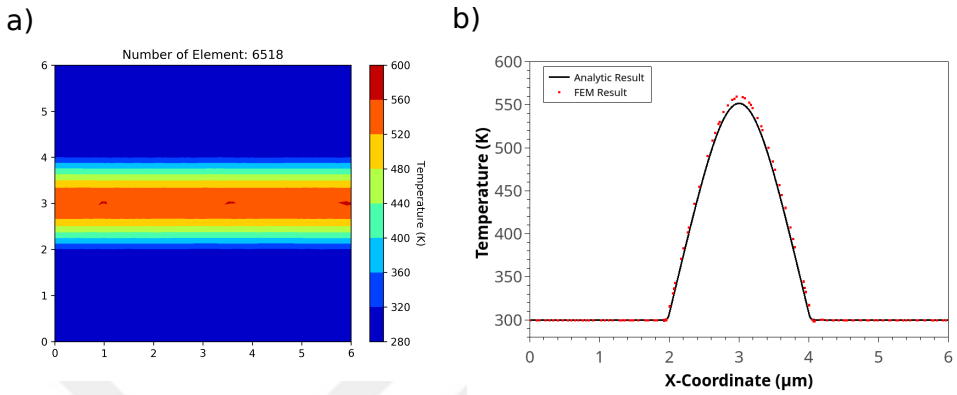

Figure 4.9: FEM Results for Anisotropic Measurement **a)**Temperature distribution of FEM result. Parameters of simulation and analytic results are as follows; trench width (2w) is 2 μm, thickness of crystal (t) is 0.65 nm, length of crystal (l_0) is 6 μm, thermal conductivity of suspended crystal (κ) is 34.5 W/mK, ratio of thermal conductivity of supported to suspended ones (ξ) is 0.9, half of the Gaussian beam width (r_0) is 0.5 μm, laser power is 0.5 mW, absorbance (α) is 2.7%, thermal transmittance (G) is 50 MW/m^{2}K and ambient temperature (T_0) is 300 K. **b)** Comparison of Analytical Solution and FEM Result. Temperature profiles are obtained from vertical direction in **a**.

Chapter 5

Result and Discussion

In the previous chapters, we have discussed how the new method works, how devices are produced for the measurement, and how resistance can give the thermal conductivity (TC) values of materials after showing solutions needed in the analysis for two configuration. However, we also have to specify whether the method gives a unique solution or not before yielding results since a resistance change might be obtained by more than one κ values in solutions. Therefore, the simulation with analytic counterpart was run for κ values from 1 to 100 W/mK (others are same with ones in previous chapter) and results are in Figure 5.1. Resistance differences (ΔR) between laser on and off states changes when TC changes and TC values give only one ΔR. The reason is that TC changes temperature distribution such that temperature of each point in hole decreases (increases) when TC is chosen as larger (smaller) than previous value as demonstrated in Figure 5.1-b. Therefore, finding ΔR by adjusting TC gives the actual TC value of the material.

However, ΔR differences between analytic and FEM results can be seen also. Variation is caused by ΔR calculation in FEM simulation. Triangles was used to mesh solution domain in FEM as shown in Figure 5.2-a. After finding temperature distribution and temperature dependent resistivity, equivalent resistance along the crystal have to be calculated in order to find ΔR. For that, the solution

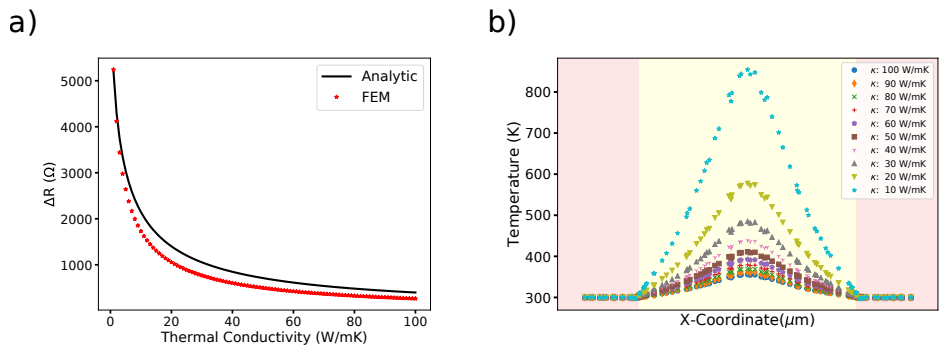

Figure 5.1: Proofs of Unique Solution by Analytic Solution and FEM Results **a)** The graphic shows that each TC value corresponds to only one ΔR so the solution is unique. **b)** Temperature profile for different TC values (κ) gives the reason of uniqueness as temperature distribution in each point decreases when TC increases. Pink area is from supported parts of crystal and yellow area is the part on hole.

area is divided by strips (black solid line in Figure 5.2-a), triangle corners in each strip are determined, distances between corners are calculated, resistivity is converted resistance by finding cross section area and accepting length as strip length. Finally equivalent resistance is found by the method of calculating the circuits equivalent resistance in mixed resistor circuits, mentioned previously, and the value is subtracted to the crystal initial resistance in order to find ΔR. Although accuracy in these calculations depends on higher number of triangles and strips; triangulation, calculation of parameters needed in each point and iteration of matrix in FEM simulation make running it with high number of points impossible with a limits of a computer memory. Highest number of elements (triangles) is $\sim$ 11000. If the same number of strips and lower in analytic solution were used, analytic ΔR changed also since probably number of strips was not enough to accurately find temperature distribution and resistance differences. This gives us maximum error margin as 17 % around 8 W/mK. This error can be eliminated by using more powerful computer system. Furthermore, if temperature distribution is checked in same TC range, FEM and analytic solution give same results as shown in Figure 5.2-b so that there is no need to suspect temperature distribution variation for the differences in ΔR.

Therefore, we have to change analysis method to obtain more reliable results.

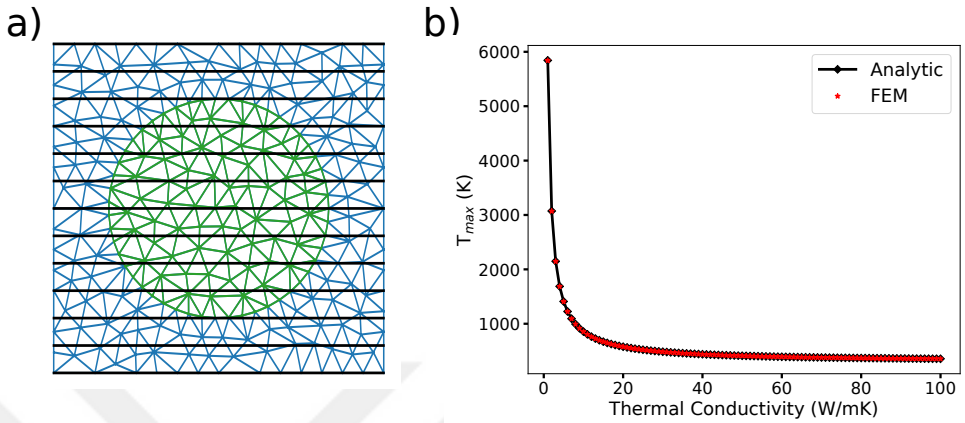

Figure 5.2: Mesh and Strip in FEM and Comparison of T_{max} **a)** A mesh-strip mechanism shows how to mesh a domain and divide by strips in FEM in order to calculate equivalent resistance after finding temperature distribution. Black line is for strip and blue shows triangles. **b)** TC values from 1 to 100 W/mK give same results in FEM and analytic solution so that FEM can be used in wide range of TC to find temperature distribution exactly.

If temperature distribution in hole area is considered, the reliability problem can be solved. Temperatures on supported parts of crystals (pieces on wafer) are equal to ambient temperature for different parameter configuration simply as shown in Figure 5.1-b. Different laser power, absorbance or crystal thickness also give the same result. Hence, temperature of supported parts can be assumed as ambient temperature directly and analytic solution for suspended parts can be used since there is a solution of heat equation for hole area by symmetry. This strategy makes calculation faster but a new meshing method is needed to utilize symmetry for resistance calculation also. Therefore, all domain is divided by square via a code written by ourselves in python. A length of squares is determined as equal to thickness of crystals so that they are divided by cubic structure in 3D. This makes temperature dependent resistance calculation possible without resistivity since length and width are same so that they are canceled each other in calculation. Moreover, number of elements can be ∼190000 and does not create not-enough-memory error so the problem about the number was be solved in this way.

$$\Delta R \simeq \frac{I_{pc} R^2}{V_{bias}} \tag{5.1}$$

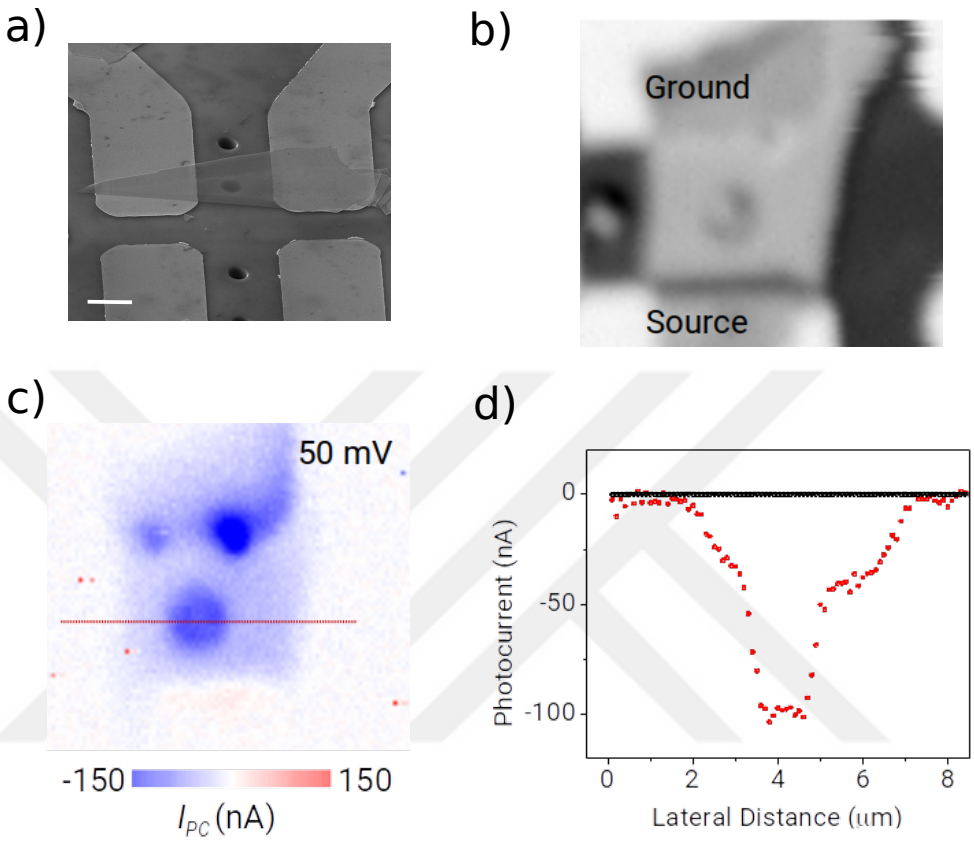

Figure 5.3: Photocurrent Measurement with Crystal Image **a)** The image shows a TaS_2 crystal used in SPCM. Scale bar is 5 μm. **b)** Reflection map is taken in SPCM to comment on photocurrent result easily. **c)** A photocurrent map by applying 50 mV bias to the crystal shows variation along the crystal and helps to obtain ΔR value from center of hole. **d)** Photocurrent profile is taken from red dash line in photocurrent map.

In the measurement, we have found resistance differences from scanning photocurrent microscopy (SPCM) to increase accuracy experimentally. SPCM makes the measurement easier due to three purposes. Firstly, it can give ΔR directly as shown in Equation 5.1 where I_{pc} and V_{bias} are photocurrent and applied voltage to the crystal. (Derivation of equation can be found in Appendix B) Secondly, SPCM is a scanning technique so it collects data from each point. If any damage or ripple exists on the crystal, SPCM shows it so that crystal quality can be determined. Thirdly, we can ensure that laser is parked in the center of hole due to SPCM since the experiment has to be performed in that place in order to obtain

equal radial temperature distribution due to radial symmetry. Many photocurrent values with reflection map by moving laser spot are collected in SPCM and ΔR value (from photocurrent) in the center is taken to calculate TC from these data set.

Figure 5.3 demonstrates such SPCM measurement as an example. The crystal is TaS_2 and was transferred on hole after exfoliation. Figure 5.3-c shows that higher resistance around contacts and holes as expected. Moreover, figure 5.3-d proves radial symmetry experimentally. Photocurrent values around center of hole are same and decreases at the edge of hole and then becomes almost zero due to cooling role of SiO_2 as heat sink as we found in the simulations.

After performing the experiments on 2H-TaS_2 devices whose thicknesses are around 30 nm, some parameters were needed to run analytic solution. Absorbance value of TaS_2 at that thickness, laser power, Gaussian beam radius for each measurement (since it might change because of laser focus) and thermal transmittance between SiO_2 and 2D materials have to be known in order to find temperature distribution. Absorbance was found as 33 % via our optical setup and laser power values were recorded during experiments as from 40 μW to 225 μW. Gaussian radii were found by curve fitting of numerical derivative data of reflection and determined from 0.7 μm to 0.9 μm. Thermal transmittance was deduced as 50 MW/m^{2}K by literature review.[8, 7] 2H-TaS_2 is a metallic material so we should determine ΔR by temperature dependency relation of resistance in metals. Thus, temperature coefficient is required and found in the literature as $\sim$0.00303 K^1.[65, 66]

Then, TC value of TaS_2 was determined as 9.55$\pm$1.27 W/mK for the first time. Figure 5.4 shows one of these crystals. Gaussian beam radius is taken as average of two different values since radius changes with laser focus and average radius value is estimated as radius on the center of hole. TC value of the sample is found as 9.39 W/mK. These values are expected since TC of 1T-TaS_2 and 2H-$TaSe_2$ are 5 W/mK and 15 W/mK at room temperature.[67] If Wiedemann-Franz law is applied to 2H-TaS_2 at room temperature, κ can be estimated as $\sim$6.5-8.5 W/mK. These values support also our findings. Therefore, the results suggest that the

resistance based TC measurement method is promising for 2D materials.

As future work, air cooling effect can be added to calculations in order to increase accuracy also. Moreover, we hope that this new method will pave the way for thermal conductivity measurement on many 2D materials so that new thermoelectric materials and heat dissipation applications can be designed.

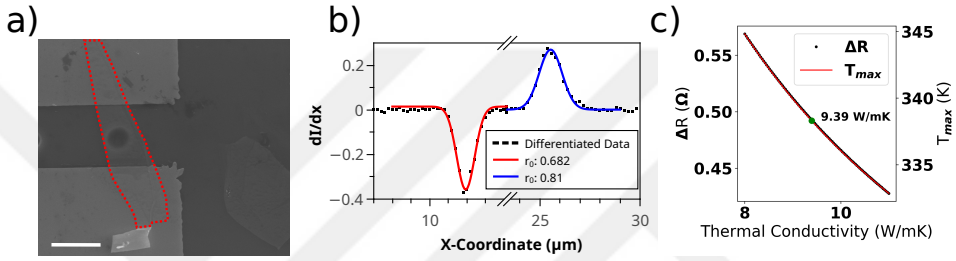

Figure 5.4: Thermal Conductivity Measurement Results **a)** Crystal image in electron microscope. Red line shows crystal edge. Scale bar is 10 μm. **b)** Finding Gaussian beam radius. A horizontal data, passing through contact and wafer, was taken from reflection map and it was differentiated numerically. Then Gaussian equation was used for curve fit. r_0 values in legend show values of Gaussian beam radius. **c)** Thermal conductivity fitting. TC values corresponding to measured ΔR are found by running codes in a TC value range.

Bibliography

[1] V. Bhatt, "What is automobile engine?," June 2013.

[2] T. L. Bergman, A. S. Lavine, F. P. Incropera, and D. P. DeWitt, *Fundamentals of Heat and Mass Transfer*. Wiley, 2011.

[3] A. A. Balandin, S. Ghosh, W. Bao, I. Calizo, D. Teweldebrhan, F. Miao, and C. N. Lau, "Superior thermal conductivity of single-layer graphene," *Nano Letters*, vol. 8, pp. 902–907, Mar. 2008.

[4] S. Chen, A. L. Moore, W. Cai, J. W. Suk, J. An, C. Mishra, C. Amos, C. W. Magnuson, J. Kang, L. Shi, and R. S. Ruoff, "Raman measurements of thermal transport in suspended monolayer graphene of variable sizes in vacuum and gaseous environments," *ACS Nano*, vol. 5, pp. 321–328, Dec. 2010.

[5] S. Ghosh, I. Calizo, D. Teweldebrhan, E. P. Pokatilov, D. L. Nika, A. A. Balandin, W. Bao, F. Miao, and C. N. Lau, "Extremely high thermal conductivity of graphene: Prospects for thermal management applications in nanoelectronic circuits," *Applied Physics Letters*, vol. 92, p. 151911, Apr. 2008.

[6] W. Cai, A. L. Moore, Y. Zhu, X. Li, S. Chen, L. Shi, and R. S. Ruoff, "Thermal transport in suspended and supported monolayer graphene grown by chemical vapor deposition," *Nano Letters*, vol. 10, pp. 1645–1651, May 2010.

[7] R. Yan, J. R. Simpson, S. Bertolazzi, J. Brivio, M. Watson, X. Wu, A. Kis, T. Luo, A. R. H. Walker, and H. G. Xing, "Thermal conductivity of monolayer molybdenum disulfide obtained from temperature-dependent raman spectroscopy," *ACS Nano*, vol. 8, pp. 986–993, Jan. 2014.

[8] X. Zhang, D. Sun, Y. Li, G.-H. Lee, X. Cui, D. Chenet, Y. You, T. F. Heinz, and J. C. Hone, "Measurement of lateral and interfacial thermal conductivity of single- and bilayer MoS2 and MoSe2 using refined optothermal raman technique," *ACS Applied Materials & Interfaces*, vol. 7, pp. 25923–25929, Nov. 2015.

[9] J. J. Bae, H. Y. Jeong, G. H. Han, J. Kim, H. Kim, M. S. Kim, B. H. Moon, S. C. Lim, and Y. H. Lee, "Thickness-dependent in-plane thermal conductivity of suspended MoS2 grown by chemical vapor deposition," *Nanoscale*, vol. 9, no. 7, pp. 2541–2547, 2017.

[10] K. S. Novoselov, A. K. Geim, S. V. Morozov, D. Jiang, Y. Zhang, S. V. Dubonos, I. V. Grigorieva, and A. A. Firsov, "Electric field effect in atomically thin carbon films," *Science*, vol. 306, no. 5696, pp. 666–669, 2004.

[11] A. P. Balan, S. Radhakrishnan, C. F. Woellner, S. K. Sinha, L. Deng, C. de los Reyes, B. M. Rao, M. Paulose, R. Neupane, A. Apte, V. Kochat, R. Vajtai, A. R. Harutyunyan, C.-W. Chu, G. Costin, D. S. Galvao, A. A. Martí, P. A. van Aken, O. K. Varghese, C. S. Tiwary, A. M. M. R. Iyer, and P. M. Ajayan, "Exfoliation of a non-van der waals material from iron ore hematite," *Nature Nanotechnology*, vol. 13, pp. 602–609, May 2018.

[12] J. R. Schaibley, H. Yu, G. Clark, P. Rivera, J. S. Ross, K. L. Seyler, W. Yao, and X. Xu, "Valleytronics in 2d materials," *Nature Reviews Materials*, vol. 1, Aug. 2016.

[13] A. M. Jones, H. Yu, N. J. Ghimire, S. Wu, G. Aivazian, J. S. Ross, B. Zhao, J. Yan, D. G. Mandrus, D. Xiao, W. Yao, and X. Xu, "Optical generation of excitonic valley coherence in monolayer WSe2," *Nature Nanotechnology*, vol. 8, pp. 634–638, Aug. 2013.

[14] A. Avsar, J. Y. Tan, M. Kurpas, M. Gmitra, K. Watanabe, T. Taniguchi, J. Fabian, and B. Özyilmaz, "Gate-tunable black phosphorus spin valve with nanosecond spin lifetimes," *Nature Physics*, vol. 13, pp. 888–893, May 2017.

[15] W.-T. Hsu, L.-S. Lu, P.-H. Wu, M.-H. Lee, P.-J. Chen, P.-Y. Wu, Y.-C. Chou, H.-T. Jeng, L.-J. Li, M.-W. Chu, and W.-H. Chang, "Negative circular polarization emissions from WSe2/MoSe2 commensurate heterobilayers," *Nature Communications*, vol. 9, Apr. 2018.

[16] W. Han, "Perspectives for spintronics in 2d materials," *APL Materials*, vol. 4, p. 032401, Mar. 2016.

[17] R. Pisoni, Z. Lei, P. Back, M. Eich, H. Overweg, Y. Lee, K. Watanabe, T. Taniguchi, T. Ihn, and K. Ensslin, "Gate-tunable quantum dot in a high quality single layer MoS2 van der waals heterostructure," *Applied Physics Letters*, vol. 112, p. 123101, Mar. 2018.

[18] D. Hsieh, Y. Xia, D. Qian, L. Wray, F. Meier, J. H. Dil, J. Osterwalder, L. Patthey, A. V. Fedorov, H. Lin, A. Bansil, D. Grauer, Y. S. Hor, R. J. Cava, and M. Z. Hasan, "Observation of time-reversal-protected single-dirac-cone topological-insulator states inBi2te3andsb2te3," *Physical Review Letters*, vol. 103, Sept. 2009.

[19] L.-D. Zhao, S.-H. Lo, Y. Zhang, H. Sun, G. Tan, C. Uher, C. Wolverton, V. P. Dravid, and M. G. Kanatzidis, "Ultralow thermal conductivity and high thermoelectric figure of merit in SnSe crystals," *Nature*, vol. 508, pp. 373–377, Apr. 2014.

[20] N. Mehmood, H. R. Rasouli, O. Çakıroğlu, and T. S. Kasırga, "Photocurrent generation in a metallic transition-metal dichalcogenide," *Physical Review B*, vol. 97, May 2018.

[21] Y. Jannot and A. Degiovanni, *Thermal Properties Measurement of Materials (Materials Science)*. Wiley-ISTE, 2018.

[22] N. Peimyoo, J. Shang, W. Yang, Y. Wang, C. Cong, and T. Yu, "Thermal conductivity determination of suspended mono- and bilayer WS2 by raman spectroscopy," *Nano Research*, vol. 8, pp. 1210–1221, Nov. 2014.

[23] S. Ghosh, W. Bao, D. L. Nika, S. Subrina, E. P. Pokatilov, C. N. Lau, and A. A. Balandin, "Dimensional crossover of thermal transport in few-layer graphene," *Nature Materials*, vol. 9, pp. 555 EP –, May 2010.

[24] Y. Xian, P. Zhang, S. Zhai, P. Yuan, and D. Yang, "Experimental characterization methods for thermal contact resistance: A review," *Applied Thermal Engineering*, vol. 130, pp. 1530 – 1548, 2018.

[25] E. Smith and G. Dent, *Modern Raman Spectroscopy - A Practical Approach*. John Wiley & Sons, Ltd, dec 2004.

[26] S. Sahoo, A. P. S. Gaur, M. Ahmadi, M. J.-F. Guinel, and R. S. Katiyar, "Temperature-dependent raman studies and thermal conductivity of few-layer MoS2," *The Journal of Physical Chemistry C*, vol. 117, pp. 9042–9047, Apr. 2013.

[27] N. Peimyoo, J. Shang, W. Yang, Y. Wang, C. Cong, and T. Yu, "Thermal conductivity determination of suspended mono- and bilayer WS2 by raman spectroscopy," *Nano Research*, vol. 8, pp. 1210–1221, Nov. 2014.

[28] H. Zhou, J. Zhu, Z. Liu, Z. Yan, X. Fan, J. Lin, G. Wang, Q. Yan, T. Yu, P. M. Ajayan, and J. M. Tour, "High thermal conductivity of suspended few-layer hexagonal boron nitride sheets," *Nano Research*, vol. 7, pp. 1232–1240, June 2014.

[29] Z. Luo, J. Maassen, Y. Deng, Y. Du, R. P. Garrelts, M. S. Lundstrom, P. D. Ye, and X. Xu, "Anisotropic in-plane thermal conductivity observed in few-layer black phosphorus," *Nature Communications*, vol. 6, Oct. 2015.

[30] J. H. Seol, I. Jo, A. L. Moore, L. Lindsay, Z. H. Aitken, M. T. Pettes, X. Li, Z. Yao, R. Huang, D. Broido, N. Mingo, R. S. Ruoff, and L. Shi, "Two-dimensional phonon transport in supported graphene," *Science*, vol. 328, pp. 213–216, Apr. 2010.

[31] M. T. Pettes, I. Jo, Z. Yao, and L. Shi, "Influence of polymeric residue on the thermal conductivity of suspended bilayer graphene," *Nano Letters*, vol. 11, pp. 1195–1200, Mar. 2011.

[32] A. Aiyiti, S. Hu, C. Wang, Q. Xi, Z. Cheng, M. Xia, Y. Ma, J. Wu, J. Guo, Q. Wang, J. Zhou, J. Chen, X. Xu, and B. Li, "Thermal conductivity of suspended few-layer MoS2," *Nanoscale*, vol. 10, no. 6, pp. 2727–2734, 2018.

[33] I. Jo, M. T. Pettes, J. Kim, K. Watanabe, T. Taniguchi, Z. Yao, and L. Shi, "Thermal conductivity and phonon transport in suspended few-layer hexagonal boron nitride," *Nano Letters*, vol. 13, pp. 550–554, Jan. 2013.

[34] B. Smith, B. Vermeersch, J. Carrete, E. Ou, J. Kim, N. Mingo, D. Akinwande, and L. Shi, "Temperature and thickness dependences of the anisotropic in-plane thermal conductivity of black phosphorus," *Advanced Materials*, vol. 29, p. 1603756, Nov. 2016.

[35] M. J. Mleczko, R. L. Xu, K. Okabe, H.-H. Kuo, I. R. Fisher, H.-S. P. Wong, Y. Nishi, and E. Pop, "High current density and low thermal conductivity of atomically thin semimetallic WTe2," *ACS Nano*, vol. 10, pp. 7507–7514, July 2016.

[36] K. T. Regner, S. Majumdar, and J. A. Malen, "Instrumentation of broadband frequency domain thermoreflectance for measuring thermal conductivity accumulation functions," *Review of Scientific Instruments*, vol. 84, p. 064901, June 2013.

[37] P. Jiang, X. Qian, and R. Yang, "Tutorial: Time-domain thermoreflectance (TDTR) for thermal property characterization of bulk and thin film materials," *Journal of Applied Physics*, vol. 124, p. 161103, Oct. 2018.

[38] D. G. Cahill, "Analysis of heat flow in layered structures for time-domain thermoreflectance," *Review of Scientific Instruments*, vol. 75, pp. 5119–5122, Dec. 2004.

[39] D. G. Cahill, "Thermal-conductivity measurement by time-domain thermoreflectance," *MRS Bulletin*, vol. 43, pp. 782–789, Oct. 2018.

[40] P. Jiang, X. Qian, and R. Yang, "Time-domain thermoreflectance (TDTR) measurements of anisotropic thermal conductivity using a variable spot size approach," *Review of Scientific Instruments*, vol. 88, p. 074901, July 2017.

[41] P. Jiang, X. Qian, and R. Yang, "Time-domain thermoreflectance (TDTR) measurements of anisotropic thermal conductivity using a variable spot size approach," *Review of Scientific Instruments*, vol. 88, p. 074901, July 2017.

[42] P. Jiang, X. Qian, X. Gu, and R. Yang, "Probing anisotropic thermal conductivity of transition metal dichalcogenides MX2 (m = mo, w and x = s, se) using time-domain thermoreflectance," *Advanced Materials*, vol. 29, p. 1701068, July 2017.

[43] H. Jang, J. D. Wood, C. R. Ryder, M. C. Hersam, and D. G. Cahill, "Anisotropic thermal conductivity of exfoliated black phosphorus," *Advanced Materials*, vol. 27, pp. 8017–8022, Oct. 2015.

[44] H. Jang, C. R. Ryder, J. D. Wood, M. C. Hersam, and D. G. Cahill, "3d anisotropic thermal conductivity of exfoliated rhenium disulfide," *Advanced Materials*, vol. 29, p. 1700650, July 2017.

[45] W. Liu and A. A. Balandin, "Temperature dependence of thermal conductivity of AlxGa1-xN thin films measured by the differential 3ω technique," *Applied Physics Letters*, vol. 85, pp. 5230–5232, Nov. 2004.

[46] D. de Koninck, *Thermal Conductivity Measurements Using the 3-Omega Technique:Application to Power Harvesting Microsystems*. PhD thesis, 2008.

[47] D. G. Cahill, "Thermal conductivity measurement from 30 to 750 k: the 3ω method," *Review of Scientific Instruments*, vol. 61, pp. 802–808, Feb. 1990.

[48] R. R. S. Chen, A.L. Moore, W. Cai, J.W. Suk, J. An, C. Mishra, C. Amos, C.W. Magnuson, J. Kang, L. Shi, R.S. RuoffS. Chen, A.L. Moore, W. Cai, J.W. Suk, J. An, C. Mishra, C. Amos, C.W. Magnuson, J. Kang, L. Shi, "Raman Measurements of Thermal Transport in Suspended Monolayer Graphene of Variable Sizes in Vacuum and Gaseous Environments," *ACS nano*, vol. 5, no. 1, p. 321, 2010.

[49] T. Wang, M. Han, R. Wang, P. Yuan, S. Xu, and X. Wang, "Characterization of anisotropic thermal conductivity of suspended nm-thick black phosphorus with frequency-resolved raman spectroscopy," *Journal of Applied Physics*, vol. 123, p. 145104, Apr. 2018.

[50] W. D. Callister, *Materials science and engineering: an introduction 8e*. John Wiley & Sons, 2012.

[51] M. B. Bhavanbhai, *Growth Of Molybdenum Dichalcogenides Using Iodine As Transport Material Characterization And High Pressure Studies*. PhD thesis, 2017.

[52] C. Kittel, *Introduction to Solid State Physics*. Wiley, 2004.

[53] T. L. Bergman and F. P. Incropera, *Fundamentals of heat and mass transfer*. John Wiley, 2011.

[54] M. Buscema, M. Barkelid, V. Zwiller, H. S. J. van der Zant, G. A. Steele, and A. Castellanos-Gomez, "Large and tunable photothermoelectric effect in single-layer MoS2," *Nano Letters*, vol. 13, pp. 358–363, Jan. 2013.

[55] Y. Zhou and K. P. Loh, "Making patterns on graphene," *Advanced Materials*, vol. 22, pp. 3615–3620, June 2010.

[56] H. Nguyen, C.-F. Huang, W. Luo, G. M. Xia, Z. Chen, Z. Li, C. Raymond, D. Doyle, and F. Zhao, "Synthesis of large-scale 2-d MoS2 atomic layers by hydrogen-free and promoter-free chemical vapor deposition," *Materials Letters*, vol. 168, pp. 1–4, Apr. 2016.

[57] M. J. Mleczko, R. L. Xu, K. Okabe, H.-H. Kuo, I. R. Fisher, H.-S. P. Wong, Y. Nishi, and E. Pop, "High current density and low thermal conductivity of atomically thin semimetallic WTe2," *ACS Nano*, vol. 10, pp. 7507–7514, July 2016.

[58] D. J. Late, B. Liu, H. S. S. R. Matte, V. P. Dravid, and C. N. R. Rao, "Hysteresis in single-layer MoS2 field effect transistors," *ACS Nano*, vol. 6, pp. 5635–5641, May 2012.

[59] R. Frisenda, E. Navarro-Moratalla, P. Gant, D. P. D. Lara, P. Jarillo-Herrero, R. V. Gorbachev, and A. Castellanos-Gomez, "Recent progress in the assembly of nanodevices and van der waals heterostructures by deterministic placement of 2d materials," *Chemical Society Reviews*, vol. 47, no. 1, pp. 53–68, 2018.

[60] A. Taube, J. Judek, A. Łapińska, and M. Zdrojek, "Temperature-dependent thermal properties of supported MoS2 monolayers," *ACS Applied Materials and Interfaces*, vol. 7, no. 9, pp. 5061–5065, 2015.

[61] Z. Luo, J. Maassen, Y. Deng, Y. Du, R. P. Garrelts, M. S. Lundstrom, P. D. Ye, and X. Xu, "Anisotropic in-plane thermal conductivity observed in few-layer black phosphorus," *Nature Communications*, vol. 6, Oct. 2015.

[62] M. N. O. Sadiku, *Numerical Techniques In Electromagnetics With Matlab, 3rd Edition*. CRC Press, 2011.

[63] H. C. Huang and A. S. Usmani, *Finite Element Analysis for Heat Transfer: Theory and Software*. Springer, 2012.

[64] D. L. Logan, *A First Course in the Finite Element Method - SI Version*. Cengage Learning, 2010.

[65] L. Li, W. Lu, Y. Liu, Z. Qu, L. Ling, and Y. Sun, "Influence of defects on charge–density–wave and superconductivity in 1t-TaS2 and 2h-TaS2 systems," *Physica C: Superconductivity*, vol. 492, pp. 64–67, Sept. 2013.

[66] L. Li, W. Lu, X. Zhu, X. Zhu, Z. Yang, W. Song, and Y. Sun, "Influence of the low mn intercalation on magnetic and electronic properties of 2h-TaS2 single crystals," *Journal of Magnetism and Magnetic Materials*, vol. 323, pp. 2536–2541, Nov. 2011.

[67] M. D. Núñez-Regueiro, J. M. Lopez-Castillo, and C. Ayache, "Thermal conductivity of 1T-TaS2 and 2H-TaSe2," *Physical Review Letters*, vol. 55, pp. 1931–1934, Oct. 1985.

Appendix A

Relation Between κ and Raman Shift

The thermal conductivity, κ, of a material is the property of its ability to conduct heat and is usually introduced through Fourier's law for heat conduction. Fourier's law is written as:

$$\begin{aligned} \vec{q} &= -\kappa \, \vec{\nabla} T \\ q &= \frac{Q}{A \, t} \end{aligned} \tag{A.1}$$

where q is local heat flux (amount of energy that flows through a unit area per unit time), κ is thermal conductivity, ∇T is local temperature gradient, A is area and t is elapsed time for measurement. If this equation is written in differential form;

$$\frac{\partial Q}{\partial t} = -\kappa \oint \nabla T.dS \tag{A.2}$$

If thermal conductivity is taken to the left side, the expression becomes;

$$\kappa = \frac{1}{A} \frac{\partial Q/\partial t}{\partial T} = \frac{L}{2A} \frac{\Delta P}{\Delta T} \tag{A.3}$$

In the denominator, 2 comes from conversion of radial heat wave to planer heat wave since calculation was done radially first, as said in *Balandin et al.* paper [23]. We want to measure temperature dependent Raman peak. Therefore, we need changing peak position depending on temperature and it is;

$$\omega = \omega_0 + \chi_T.T \qquad \Rightarrow \qquad \Delta T = \Delta\omega/\chi_T \tag{A.4}$$

If we insert that result into Equation A.3, the relation becomes;

$$\kappa = \chi_T \frac{L}{2hW} \frac{\partial P}{\partial \omega} \tag{A.5}$$

where L, h, W are length, thickness and width of the crystal respectively.

Appendix B

Relation Between I_{pc} and ΔR

Photocurrent(I_{pc}) is created by excitation of laser beam and it can be defined as current created by photon interaction. It is equal to current differences between laser on and off state like

$$I_{pc} = I_{on} - I_{off} \tag{B.1}$$

If the currents are written in a voltage-resistance form due to Ohms law

$$I_{pc} = \frac{V_{bias}}{R + \Delta R} - \frac{V_{bias}}{R} \tag{B.2}$$

where R is crystal resistance in laser-off state, V_bias is applied voltage and ΔR is resistance change due to laser heating. We need to ΔR in order to find thermal conductivity value (κ) of the crystals. Therefore, the equation becomes

$$I_{pc} = \frac{V_{bias}\Delta R}{R(R + \Delta R)} \tag{B.3}$$

If R inside the parenthesis in denominator is brought outside, it becomes

$$I_{pc} = \frac{V_{bias}\Delta R}{R^2\left(1 + \frac{\Delta R}{\cancel{R}}\right)} \tag{B.4}$$

since ΔR is very smaller than R, it can be canceled in denominator. Then, ΔR can be found as

$$\boxed{\Delta R \simeq \frac{I_{pc}R^2}{V_{bias}}} \tag{B.5}$$